Revision 3

Reducing epistemic and model uncertainty in ionic inter-diffusion chronology: A 3D observation and dynamic modeling approach using olivine from Piton de la Fournaise, La Réunion

Fiona K. Couperthwaite[1], Daniel J. Morgan[1], Matthew J. Pankhurst[2,3], Peter D. Lee[4,5], James M. D. Day[6]

[1]School of Earth and Environment, University of Leeds, Leeds, LS2 9JT, UK

[2]Instituto Tecnológico y de Energías Renovables (ITER), 38600 Granadilla de Abona, Tenerife, Canary Islands, Spain.

[3]Instituto Volcanológico de Canariaes (INVOLCAN), INtech, La Laguna, Calle Rectora María Tejedor Salguero, 35, 38320 San Cristóbal de La Laguna, Tenerife, Canary Islands, Spain.

[4]Research Complex at Harwell, Rutherford Appleton Laboratories, Didcot, OX11 0FA, UK

[5]Mechanical Engineering, University College London, Gower Street, London, WC1E 6BT

[6]Geoscience Research Division, Scripps Institution of Oceanography, UC San Diego, La Jolla, CA, 92093, USA

*Fiona K. Couperthwaite now at College of Earth, Ocean and Atmospheric Sciences, Oregon State University, 104 CEOS Administration Building, Corvallis, OR 97331-5503

Abstract

The modeling of ionic diffusion in natural crystals has been developed over the last three decades to calculate timescales of geological processes. As the number of studies and the size of datasets have expanded, improvements in precision of the general technique are needed to resolve temporal patterns that would otherwise be masked by large uncertainties. This contribution examines fundamental aspects of timescale calculation uncertainty using Mg-Fe zonation in olivine crystals from a Piton de la Fournaise oceanite erupted in 2002CE. First, we quantitatively consider the role of geometric uncertainty in datasets, from the perspectives of sectioning angle, crystal shape and crystal agglomeration. Second, we assess how crystal growth and changing boundary conditions during diffusion pose problems for simplistic, 1-D, diffusion-only modeling.

An initial database of 104 timescales (7-45 days) was generated using typical, 1-D, isothermal diffusion-only methods for profiles taken from 30 compositionally- and texturally-zoned crystals of olivine. The initial simplistic modeling yields poor model fits and imprecise timescales; prior to this work we would have rejected >60% of these data.

Universal-stage measurements of crystal boundary angles and three-dimensional (3D) X-ray microcomputed tomography observations of crystal shape address geometric uncertainties. U-stage measurements show that, contrary to expectations of random sectioning, most boundaries modelled initially were close to the ideal sectioning plane. Assessment of crystal morphology from 2D thin sections suggests olivine crystals are dominantly euhedral, however, 3D imaging reveals that they are significantly subhedral and often exist as agglomerates, an observation which underscores both the potential for diverse crystal interactions through time in the magma

(Wieser et al., 2019), and out-of-plane effects capable of influencing calculations of diffusion profiles.

Refinements to timescale determination can be made using dynamic 1-D modeling code to resolve growth and changing boundary effects simultaneous with diffusion. We incorporated temperature-dependent crystal growth rates (both linear growth and quadratically-increasing, with a peak growth rate ~1.9×10^{-11} ms^{-1}) and temperature-dependent boundary conditions (controlled using a cooling rate of -0.5 ±0.1 ºC/hr) to remodel 13 timescales. The result was significantly improved fits of the diffusion model to the initial data, better agreement between different faces of the same crystal and less scatter within the whole dataset.

The use of 3D imaging and the inclusion of changing boundary conditions and crystal growth for diffusion calculations will enable more robust conclusions to be drawn from similar data in the future. Accurately retrieving timescale information from these crystals expands the pool of data available and reduces sampling bias towards 'well-behaved' crystals.

KEYWORDS: Olivine; diffusion chronometry; epistemic uncertainty; analytical uncertainty; Piton de la Fournaise

Introduction

Understanding of magmatic plumbing systems has been considerably advanced in recent years by investigation of individual crystal histories using quantitative diffusion chronology methods (Costa and Dungan, 2005; Morgan et al., 2006; Kahl et al., 2011; Charlier et al., 2012; Shea et al., 2015a; Hartley et al., 2016; Pankhurst et al., 2018b; Ruth et al., 2018; Petrone et al., 2018;

Mutch et al., 2019). The essential observations underpinning these studies are that chemical disequilibria within natural crystals are often partially-relaxed towards full equilibrium: a homogeneous distribution of elements (Figure 1a). Timescales are calculated by modeling a diffusion profile that fits the observed profile (Costa and Morgan, 2010).

Knowledge of ionic diffusivity in mineral lattices is gained from laboratory experiments (Buening and Buseck, 1973; Chakraborty et al., 1994; Lesher, 2010). These diffusivity calculations are attended by inherent uncertainty, which can be attached to modeled results from natural data. These experiments are designed to control environmental conditions and geometric relationships in order to provide unambiguous results (Costa et al., 2008; Brady and Cherniak, 2010; Chakraborty, 2010; Dohmen and Milke, 2010). However, it cannot be assumed that nature is so well-behaved i.e. disequilibrium conditions may be prevalent across the system and subhedral, aggregated crystals may be present. Variations in intensive parameters such as temperature, pressure (Blundy and Cashman, 2008), composition (Dohmen and Chakraborty, 2007a and b; Dohmen et al., 2007) and the geometric relationships of crystals (single crystals versus aggregates, degree of euhedrality) are central to how igneous rocks are formed (Welsch et al., 2013; Shea et al., 2015a). Application of experimental results to natural systems, while assuming these parameters are invariant, will likely lead to inaccuracies.

This contribution aims to improve the utility of diffusion studies in natural rocks by investigating effects of three common sources of analytical and epistemic uncertainty in natural systems. These are: 1) sectioning angle; 2) 3D crystal shape; 3) crystal growth and changing boundary conditions. We use Fe-Mg inter-diffusion in natural olivine as our case study, as it has a well-defined and accepted diffusivity behaviour (Dohmen and Chakraborty, 2007and b; Dohmen et al., 2007; Costa et al., 2008; Kahl et al., 2013; Bouvet de Maisonneuve et al., 2016;

Lynn et al., 2017) and because basalt petrogenesis is relatively simple. The type of improvements we discuss, however, are equally applicable in other minerals and more complex igneous systems.

We began by constructing a dataset of core-rim composition profiles using traditional methods, see Figure 1b. From these profiles, a diffusion chronometry dataset was generated whereby a single temperature is input into a 1D or 2D diffusion model, and solutions corrected for anisotropy (Costa and Chakraborty, 2004; Kahl et al. 2011; Hartley et al., 2016; Morgado et al., 2017; Pankhurst et al., 2018b), Figure 1c. We then made observations using a universal stage, X-ray microcomputed tomography (XMT) and a modeling program that can accommodate dynamic boundary and temperature conditions. Uncertainties within the chronometry dataset are then defined and corrected for by applying more advanced methods of observation and the advanced model.

With the benefit of uncorrected, and corrected datasets, we assess the influence of sectioning angle, crystal shape and crystal growth and changing boundary conditions at both a crystal scale and at a population scale. This work is complementary to the theoretical study of geometrical uncertainties and their effects on the accuracy of timescales demonstrated in Shea et al. (2015a). Whilst Shea et al. (2015b) discriminated between growth and diffusion within a classic skeletal olivine crystal, further validation requires diffusion-based studies that aim to retrieve timescales from a wider pool of natural crystals. The olivines here are at a late stage of crystal formation, the timing of the chemical profiles occurring after post-textural ripening to their observed form.

Sampling and Geological Setting

Piton de la Fournaise (PdlF) is a basaltic shield volcano forming the south-eastern portion of La Réunion, one of the Mascarene Islands that lie ~800 km off the coast of Madagascar (Longpré et al., 2006; Lénat et al., 2012), see Figure 2. There have been multiple eruptions in nearly all decades since historical records began in 1640 (*Global Volcanism Program*). Recent eruptions have occurred in 1990, 1991, 1992, 1998-2010 and 2014-present. The recent activity is mainly confined to the central caldera – Enclos Fouqué and from the northeast and southeast rift zones (Lénat et al, 2012).

The November 2002 eruption (Figure 2) occurred on the eastern flank as a lava flow (Longpré et al., 2006). The eruptive period is divided by Longpré et al. (2006) into five eruptive episodes defined by periods of inflation/deflation at the summit and the flanks and increased or decreased seismicity, related to dyke injection within the eastern flank (Longpré et al., 2006). The lava flow is comprised of oceanite (a term first introduced by Lacroix, 1923 from Peltier et al., 2009), formally defined by Boivin and Bachelery (2009) as "*a melanocratic variety of picritic basalt made of numerous large crystals (> 20%) of olivine and a lesser proportion of clinopyroxene, in a matrix enclosing microscopic crystals of augite, olivine, oxides and plagioclase*".

We sampled the 2002 lava flow from a road-side outcrop at Lat. -21.13136S, Long. 55.48424E at 223 feet elevation. This lava contains abundant 2-3 mm olivine crystals. The sample collected is denoted "RU0701" throughout the paper, and whole-rock geochemical information for this sample, including major-element composition, was reported in Peters et al. (2016).

Initial Methods

Sample preparation and characterisation

Three thin sections were cut to 48 mm × 26 mm × 35 μm, ground, and polished with colloidal silica to give sufficiently defect-free finish suitable for electron-backscatter diffraction (EBSD) analysis, as in Lloyd (1987). Within each thin section (RU0701_1-3), we refer to an individual olivine crystal using a letter and use a number to refer to a unique compositional profile extracted from that crystal for the modeling, for example: RU0701_1_A1. A scan of each thin section is included in Supplementary Data A. Mineralogical modal abundance was calculated using '*JMicrovision*' as applied to scanning electron microscope images in addition to visual assessment of olivine shape made in both 2D and 3D. A core (diameter = 1.5 cm, length = 10 cm) was taken from the bulk-rock sample using a radial drill corer at the University of Leeds, in preparation for X-ray microcomputed tomography scanning.

Scanning electron microscope and electron probe microanalysis

Backscattered electron (BSE) images of thin sections were collected for textural assessment and for composition calibration using a FEI Quanta 650 Field Emission Gun-Environmental Scanning Electron Microscope (SEM) at the University of Leeds. The imaging was conducted using a focused spot size and an accelerating voltage of 20 kV. An Oxford Instruments electron backscatter diffraction system using a *hkl Systems Nordlys* detector was used to gather crystallographic orientation data from the portions of olivine used for compositional profiling. These data were reduced using Oxford Instruments *Channel 5* software to a single set of Euler angle rotations per grain, and an in-house *MS Excel* worksheet was used to transform these into a set of a- b- and c-axis orientations relative into the EBSD analytical plane (i.e. the thin section plane).

158 Compositional rim-to-core traverses from the olivine grains were measured using a
159 JEOL JXA8230 Electron Probe Microanalyser (EPMA) equipped with five wavelength-
160 dispersive spectrometers (WDS), also at the University of Leeds. Spot sizes of 5 μm were used
161 to extract a profile perpendicular to the crystal edge at 5-10 μm intervals. The broadest diffusion
162 margin of the crystals measured is ~80 μm.

163 Multiple runs were conducted to build the full dataset, using slightly different beam
164 conditions (15-20 kV and 30-50 nA) and on-peak count times (30-60s for Ni and Mn, 30-40s for
165 Si, Fe, Al and Mg and 20-30s for Cr). Higher energy and currents were used together with
166 shorter count times and resulted in similar precision, as calculated using data from secondary
167 standards from each run. Analyses that recorded totals outside 98 to 101.1 wt% were rejected.
168 Microbeam reference materials distributed by the Smithsonian Institute, Washington D.C.
169 (Jarosewich, 1980) were used as primary standards, whose details along with detection limits
170 determined in this study are reported in Supplementary Data A.

171 The San Carlos olivine standard NMNH 111312-44 was used to calculate the external
172 accuracy and reproducibility of olivine composition via analyses at the start, end and within-run.
173 The Fo content of the San Carlos olivine was reproducible within-run precisions of 2σ = 0.07-
174 0.14 mol% (n= 66 over the course of the study). Internal olivine standards used were
175 Springwater (USNM 2566) and Geo2 (see Pankhurst et al. 2016). Analyses of groundmass
176 minerals were conducted alongside suitable matrix-matched standards, as detailed in
177 Supplementary Data A.

178

179 **Initial modeling**

Thermometry and Oxygen Fugacity. For mafic magmas it is common to utilize olivine-melt thermometry (Putirka, 2008) to determine crystallisation temperatures. In the absence of preserved homogeneous glass, we retrieved bulk compositions of the microcrystalline groundmass (Geiger *et al.*, 2016). A quantitative mapping, raster matrix method was used to collect the compositional data, using the 'Probe for EPMA' software (Donovan et al. 2012) and further refined using Surfer Software.

Grids of the groundmass were scanned using WDS, after which a matrix correction was applied to the data on a pixel-by-pixel basis, mimicking beam defocusing (another technique used to analyse broad areas; Morgan and London, 1996). The raster matrix method has the advantage of analysing large areas without the beam attenuation and spectrometer viewing angle problems associated with using wide-area defocusing (Reed, 2005). The MgO content (in wt%) derived from the raster matrix, was input into the Helz and Thornber (1987) liquid-only thermometer. This thermometer has been widely implemented to investigate the thermometry of PdlF lavas in previous studies e.g., Clague and Denlinger (1994); Famin et al. (2009); Bureau et al. (1998); Boivin and Bachèlery (2009). Uncertainties presented in this study incorporate both the internal uncertainty of +/- 10°C inherent to the thermometer as well as the MgO variability obtained via the groundmass analysis. Quantitative groundmass maps and calculation of their uncertainty can be found in Supplementary Data A. We set the oxygen fugacity at the NNO+1 buffer. A detailed explanation of this choice is included in Supplementary Data B.

Timescale calculations. Profiles of greyscale values from BSE images were extracted perpendicular to the crystal edges using *Image J* (Schneider et al., 2012), illustrated in Figure 1b. The greyscale values were calibrated to the major element compositions (Costa and Morgan,

2010) obtained from analyses of the same olivine crystal using the EPMA. Best fit diffusion profiles were then modelled for these profiles using the same numerical methods as previous work by Hartley et al. (2016), Pankhurst et al. (2018b) and Couperthwaite et al. (2020). A demonstration and explanation of the methods of the simple diffusion model used is supplied in Supplementary Data C.

Initial results

Olivine composition and textures in two dimensions

Whole-rock (XRF) compositional data for RU0701 (Supplementary Data A), plots in the range for an ultra-mafic/basaltic (SiO2 wt% <45%) rock with a high MgO content (23.5 wt%), consistent with the petrographic identification as oceanite (8-28 wt% MgO, Lacroix, 1936). The large olivine crystals that are the main focus of this study appear as mostly euhedral, occasionally embayed, crystals up to 2-3 mm in size, at ~25% modal abundance. There are approximately 300-400 olivines in each thin section. They are contained within a finer-grained groundmass (~50-80 μm) made up of clinopyroxene (40%), olivine (10%), plagioclase feldspar (50%) and spinel (5%) (see Figure 3), and often contain plagioclase inclusions in their margins. Olivine ~40 – 200 μm in size is also present (Figure 3); much smaller than the population of large crystals.

The large olivines have core compositions of Fo84 (Fo = 100*Mg/Mg+Fe+Ni+Mn), consistent with previous olivine measurements for RU0701 (Füri et al., 2010), and Fo rim compositions ranging from Fo_{75-65} (normal zonation) with what is recognisable as diffused zones

typically ~80 μm thick (Figure 3). The olivine rims are similar to the groundmass olivine composition (~Fo_{65}).

External Modeling Parameters and Timescale Uncertainties

A temperature of 1126°C (±10°C) was calculated using the average MgO (5.55 MgO wt%) of four quantitative groundmass maps (values range between 4.9 and 6.5 ±0.5 wt% MgO; Supplementary Data A). This estimated temperature is in good agreement with that used by Boivin and Bachèlery (2009), who calculated temperatures usually between 1110-1150°C (and up to 1172°C, with an interquartile range of 33°C) for various eruptions from 1977 to 1998. We set the fO_2 at NNO + 1 log units.

The initial condition was defined using the core composition Fo_{84}, with a variation in the boundary condition inferred from the rim composition between $Fo_{75\text{-}65}$ depending on the profile being modelled. The average uncertainty of each calculated timescale is 0.38 log units (1σ), calculated considering the uncertainty on temperature, activation energy and the pre-exponential factor that relates to crystal structure, jump frequency and distance (Dohmen and Chakraborty, 2007a and b; Dohmen et al., 2007).

Initial Fe-Mg diffusion timescales

Diffusion timescales (n=104) were calculated for Fe-Mg inter-diffusion in the large, zoned olivine crystals (n=30). One profile was extracted from each available face of a single crystal and/or was taken along each diffusion direction (relative to crystallographic orientations) within a crystal. An example of a diffusion model fit to a crystal compositional profile is shown

in Figure 1 b-c (further profiles are shown in Supplementary Data A). Our diffusion model best-fits can be grouped into three types:

i) Thirty-nine profiles that show a very good fit with simple modeling and can be simply explained by diffusion with a fixed boundary condition and no crystal growth

ii) Five profiles that show a poor fit to the simple model, indicated by an enhanced curvature of the diffusion profile away from the core, relative to the simple model

iii) A further 60 profiles that appear to be affected by enhanced curvature (as in ii) and a point of inflection in the profile gradient towards the rim. An example of ii) and iii) are illustrated in Fig 1c.

All initial modeling accounts for diffusion anisotropy and compositional dependence using the diffusivity data of Dohmen et al. (2007) and Dohmen and Chakraborty (2007a and b). The majority of calculated timescales range from 7 to 45 days (Figure 4). Outliers (4% of the dataset) reach 60-104 days. These longer timescales do not appear to have any relationship with the composition of cores or rims, or crystal size. Of particular note is the scatter amongst the timescales both between crystals *and* within crystals (Figure 4) i.e. even accounting for anisotropy and composition dependence. Individual crystals do not consistently correct to a singular diffusion timescale.

Initial Discussion

Scatter within the diffusion timescale dataset

Scatter between and within crystals could at least partly be due to each individual crystal petrogenesis. It cannot be assumed that the diffusion clock in each crystal was set synchronously and so it is not expected that they should form a timescale 'event', as has often previously been inferred in prior diffusion studies. Since each profile is already corrected for anisotropy, the scatter *within* crystals is therefore likely to be attributable to sectioning effects, simultaneous crystal growth and changing boundary condition effects and out-of-plane-diffusion effects (Shea et al., 2015a), as discussed in the following sections.

Sectioning angle

The ideal crystal sections to study for retrieval of accurate diffusion timescales are those that cut through the centre of a crystal and also perpendicular to at least one crystal face (and therefore also perpendicular to the diffusion front; Pearce, 1984). Thin sections cut such that crystals are not sectioned in this way (giving shallow sections) will lead to an *apparent* lengthening of the observed profiles (Costa and Chakraborty, 2004; Costa et al., 2008; Costa and Morgan, 2010; Shea et al., 2015a), which is an assumption that is often not explicitly declared or corrected for. This artificial lengthening contributes to an epistemic uncertainty on the timescale introducing a stretch factor to the traverses, most often inducing positive scatter into the timescale dataset.

Choosing the narrowest profile within a crystal should be favoured to minimise this source of error (Costa et al., 2003; Costa and Dungan, 2005; Costa et al., 2008; Costa and Morgan, 2010; Shea et al., 2015a). In practice, however, this is not always possible. Crystals picked from tephra and set in grain mounts are often fragmented, and sometimes only one crystal margin is observed, so no relative comparisons can be made. Features such as melt and mineral

inclusions, cracks, polishing defects, sub-grain boundaries or embayments in the crystal considered may further limit options for extracting a profile.

Pearce (1984) calculated the probability of obtaining an ideal cut section of a crystal for the study of zoned crystals. The probability of a section to be within 40% of the centre of a crystal, that is also within 10° of perpendicular to any one of the three major faces would be around ~20%. This implies a significant proportion of sections are likely to not meet these criteria and be affected by off-centre or shallow sectioning. Better representation may be expected, however, when considering larger crystals with a narrower rim thickness, akin to the PdlF olivines in this study. Since sectioning effects are rarely measured and incorporated into diffusion datasets (e.g., Martin et al., 2008; via U-stage measurements) this factor clearly carries some potential as a source of uncertainty.

3D texture

Out-of-plane features that may influence the development of diffusive chemical profiles include proximity to other crystals or vesicles, or low-angle adjacent crystal faces removed during the thin section process where cuts are quite off centre and almost graze a face. Crystal morphology may lead to isolated and apparently distinct crystals in thin section that in reality are connected to parts of the same crystal (Welsch et al., 2013). Such crystals might be separately analysed, and therefore be over-represented in a subsequent dataset. Without 3D context, these scenarios represent another source of epistemic error at the scale of single-crystal histories that deserves consideration, which is becoming more widely adopted as a focus for research (e.g. Jerram et al., 2018).

311

312 **Simultaneous crystal growth and changing boundary conditions with diffusion**

313 Profiles with an enhanced curvature of the diffusion profile away from the crystal core, relative
314 to the simple model and which also exhibit an inflection point in the profile gradient near the
315 crystal rim (e.g. that in Fig. 1c) are suspected of being affected by crystal growth and/or
316 changing boundary conditions simultaneous with diffusion. These profiles would normally be
317 rejected from further consideration as they do not meet quality control criteria for the degree of
318 match. For instance, the rejection rate would be ~60% for this dataset (Supplementary Data A).
319 These profiles, however, do contain valuable information with regards to the environment in
320 which they resided i.e. a change in ambient conditions. Their rejection therefore constitutes a
321 bias, whose impact on both the chronometry and petrographic interpretation is typically ignored.
322 This study attempts to recover this information through dynamic modeling.

323

324 **Advanced Methods**

325 **Calculating shallow sectioning effects**

326 The stretching of a compositional profile due to shallow sectioning, as illustrated in
327 Figure 5, can be corrected for using the following equation (Costa and Morgan, 2010);

328 $$l_m = \frac{l_t}{\cos\theta} \qquad (1)$$

329 where l_m is the measured traverse length, l_t is the true traverse length and the angle θ is the angle
330 between the crystal boundary and the normal to the sectioning plane – the 'hade'(Costa and
331 Morgan, 2010). We measure this angle using a Universal Stage (U-Stage), the operation of

which is described in Kile (2009). The shallower the cut, and hence the larger the value of θ, the more significant the stretch factor on the timescale.

The large size of the olivine grains we used for this study relative to the diffusion scale means that sections could be considerably off centre without varying the crystal face intersection angles. Stretch factors were calculated for our dataset using the angles measured with the U-stage. At a population level, this serves to highlight how shallow sectioning combined with traditional in-section-plane diffusivities would affect the PdlF diffusion dataset overall, and therefore, the possible effects on other datasets. These measurements were repeated to assess uncertainty. Much of the U-stage dataset was also re-measured independently by FKC and DJM; the results were found to be reproducible within ±5° by different operators. The stretch factor, stretched timescales and timescale shift to be applied to timescales modelled by diffusion (that are uncorrected for shallow sectioning) for a range of angles between the minimum and maximum of those measured from this dataset can be found in Supplementary Data A.

Understanding crystal shape using X-ray Microtomography

Detailed methodology of the XMT analytical procedure can be found in Supplementary Data B. Crystals and their textural context were observed in-situ in 3D within a rock core using the XMT 3D imaging. We use image segmentation software to segment the olivine crystals from the groundmass within the images produced. To capture, examine in detail, and quantify the shape of the larger (2-3 mm) olivine crystals, a number of image segmentation methods were tested. Ten slices evenly distributed through the image stack were selected, and imaged olivine belonging to large crystals was manually digitised from each slice. The advantage of scrolling above and below the slice (using a z-stack of the image) allowed us to denote olivine as belonging to a large

crystal or not, even if the slice intersected only a small area and would otherwise be indistinguishable from groundmass olivine.

'*K-means clustering*', '*watershed*' and '*trainable weka*' segmentation modules were applied to these same slices within Image J. K-means clustering partitions a dataset into k-groups (clusters). The plugin performs pixel-based segmentation based only on clusters discovered within the image (Wagstaff et al., 2001). The watershed segmentation method considers the input image as a topographic surface, with the brightness of each point representing its height. The entire relief is flooded, and dams or barriers are formed where similar pixels are found, with all similar points forming a catchment basin (Soille and Vincent, 1990). The trainable weka segmentation methods combine machine learning algorithms with image processing, assigning areas of interests to 'classes' forming the training dataset (Arganda-Carreras et al., 2017). The classifier uses a random forest algorithm and decision trees to ultimately classify the selection (Breiman, 2001; Hastie et al., 2008).

The brightness and texture of the pixels that make up the olivine are exploited for each segmentation method. Each method was optimised using the 2D slices with manually segmented olivine, to choose the best method to be applied to the entire stack. In each case the result is a binary image that approximates the location of olivine belonging to large crystals. Figure 6 illustrates the good agreement between the percentage area of olivine using all three 3D segmentation methods compared to the percentage area of olivine within the raw 2D slices. We chose to apply the trainable weka segmentation method across the 3D stacks as this method enabled full automation of each step in the methodology.

Dynamic modeling of crystal growth, changing boundary conditions and diffusion

In order to evaluate the potential changes that occur during crystal growth with simultaneous diffusion we consider two scenarios:

- That the crystal may grow, and that the outside boundary condition is mobile in space as crystallisation proceeds
- That the equilibrium composition of the olivine is changing as crystallisation proceeds, due to melt evolution

In these cases, the growth of a crystal and the change in equilibrium value are driven by changes in magma temperature and the degree of crystallisation that this affords. Because diffusivity is a strong function of temperature, we must also consider;

- That the diffusivity will be controlled by temperature, which will decrease during crystallisation down a liquidus, and
- The thermal effects on oxygen fugacity.

In order to constrain this series of processes, we chose to model diffusion over the crystallisation path of the system as a function of temperature, to obtain the equilibrium olivine values at any given temperature which can be applied as a boundary condition. By specifying a cooling rate applied to the sample, this can be expected to control the evolution of the external melt composition with time and control the diffusivity as a function of time. What the diffusion modeling requires is a precise starting melt composition, which can be modelled using software such as Petrolog3 (Danyushevsky and Plechov, 2011) or MELTS (Ghiorso and Sack, 1995; Asimow and Ghiorso, 1998). We used Petrolog3 to determine the initial melt composition prior to olivine rim growth and groundmass formation. We extracted variable amounts of Fo_{84} olivine from the whole-rock composition and assessed olivine-melt equilibrium. We then project

crystallisation of this melt considering the phases present in the observed assemblages (with the exception of orthopyroxene, which is present in low abundances in the Petrolog3 models). A detailed methodology is described in Supplementary Data B.

Thermodynamic modeling using Petrolog3. Olivine in the models typically crystallises through the interval Fo_{84-79}, but more evolved olivine is not present on the liquidus; it is replaced in the models by orthopyroxene, which crystallises at the level of a few percent. This is distinct from what we see in the specimens, where no orthopyroxene is observed, and olivine rims exhibit compositions down to Fo_{65} or less (indicated by brighter BSE pixels at the very rim, below the spatial resolution of the EPMA). We suspect this represents a limitation in the modeling versus nature; either the nucleation of orthopyroxene is somehow suppressed in the natural samples, or that the crystals are so small as to be visually unidentifiable from olivine within the fine-grained groundmass. Regardless, orthopyroxene does not form overgrowths on olivine in RU0701 and as such there is no evidence to support its inclusion across the petrogenetic interval of interest. Therefore, we excluded orthopyroxene from the Petrolog3 modeling, restricting the assemblage to olivine, plagioclase, clinopyroxene and oxide. Olivine crystals in natural samples have been able to exchange via diffusion with an adjacent, more-evolved melt that equilibrate with Fo_{65}, since fractionation to a cumulate has not occurred.

Figure 7 shows how crystallisation behaviour changes with temperature in the model. This curve is parameterised for use in a diffusion model – each stretch of cotectic is fitted with a third order polynomial with $R^2 > 0.99$, which is used within that temperature range to determine the equilibrium olivine composition for any given temperature. Note that at temperatures below

1117ºC, olivine does not crystallise within the model, and the values reflect the equilibrium due to exchange with an evolved ambient melt and a K_d for olivine of 0.303.

Dynamic Diffusion modeling. The modeling was conducted using a simple, iterative one-dimensional finite difference model, whose logic follows that shown in Figure 8. In this manner, the model allows for tracking the liquidus and an evolving melt, allowing the temperature to control both the composition, the diffusivity, and the absolute oxygen fugacity (via a buffer), much as it would during the cooling of the magma.

Advanced Results

Sectioning effects

Our analysis of sectioning effects shows a large frequency of sections cuts within angles 10° of vertical and a smaller frequency of the very shallow angles (where the crystal edge is sectioned up to 30° to the vertical; Figure 9). These angles correspond to timescale shortening between 0-2.5 and 33.3% relative. The average angle measured from vertical (the "sectioning" angle) for the PdlF dataset is 8.9º and would require an average shift of ~2.5% applied to the timescale dataset (0.011 log units), which is low, relative to other sources of uncertainty. A full list of measured angles and the corresponding shift on individual timescales is included in Supplementary Data A.

Quantification of 3D crystal shapes

3D renders of four olivine crystals or crystal aggregates are shown in Figure 10. A further 25 crystals are provided in Supplementary Data A. Assessment of these images reveals that only

445 25% of the crystals could be considered euhedral; 68% are subhedral, and 7% are anhedral.
446 Furthermore, only 25% are individual crystals and the remainder are present as crystal
447 agglomerates. These agglomerates are generally crystallographically aligned (see Figure 10 (e)).
448 Nearly all the crystals are polyhedral, apart from two that are tabular shaped; 19% are rounded
449 nodules and 13% of the agglomerates show parallel organisation or hierarchy as described by
450 (Welsch et al., 2013).
451
452 **Crystal growth and changing boundary condition incorporated into diffusion timescales**
453 Using the initial melt composition from Petrolog3 (see Figure 7), we ran a number of diffusion
454 models (as described in Figure 8) to assess the effects of changing boundary conditions and
455 crystal growth on diffusion timescales. The results of each are described in the following
456 sections.
457
458 **Modeling sequence 1: changing boundary condition (no growth).** Modeling was
459 initially conducted for a starting temperature of 1126ºC, at NNO+1, for a variety of cooling rates.
460 This generates a sequence of diffusion curves with geometries as shown in Figure 11. The
461 profiles follow proportionally similar trajectories through temperature and time, are self-similar
462 and display typical proportionality for diffusion profiles, i.e., where cooling rates quadruple, the
463 diffusion width decreases by a factor of two.
464
465 **Modeling sequence 2: changing boundary condition with growth.** Modeling was also
466 conducted for a starting temperature of 1126ºC, at NNO+1, for a single cooling rate of -1 ºC/hr,
467 combined with a variety of growth rates. This generates a sequence of diffusion curves with

468 geometries as shown in Figure 12; the addition of growth stretches the profiles, as would be
469 expected. As growth is considered here to be linear in time, and diffusion is reducing
470 exponentially due to linear cooling in time, the profiles are decoupled, and are not self-similar.
471 The highest growth rates are in effect recording a dominance of the liquidus surface, which is not
472 completely smooth, and which has been subjected to a variable degree of diffusional smoothing
473 with distance.

474

475 **Modeling sequence 3: fitting a specific case.** Due to the dynamic interplay of
476 parameters, an initial profile was considered for detailed investigation using these diffusion and
477 growth models. The fitting was performed iteratively by changing the relative magnitude of
478 cooling rates and growth rates to gradually improve the fit for a particular traverse. To allow for
479 an appreciation of both the similarity and difference between the curves in Figures 11 and 12,
480 and real data, we superpose a profile onto these curves (labelled 'measured').

481 These figures show that natural data is significantly divergent from both cases studied,
482 though growth allows us to fit the broader rim. A particular feature of the natural curve is that it
483 has a gradual concave curvature, while the diffusion-only curves are convex. Such concavity is
484 consistent with increasing growth rates; this can be seen on Figure 12, as the best fit seems
485 consistent with high growth rates at the rim, but with lower growth rates near the core. Crystals
486 therefore seem to have experienced a late-stage, accelerating rim growth. This was considered by
487 applying a temperature-dependent growth across a temperature range such that:

488 $$G_{T,t} = 2G_0\left(\frac{T_0 - T}{T_0 - T_{min}}\right)$$

Where G is the growth rate, G_0 the half growth rate at G_{min}, T_0 is the start temperature and T_{min} is a nominal finish temperature. This produces a gradually-increasing growth rate following a parabolic curve. By adjusting the parameters of cooling rate and the parameter G_0, above, we can attempt to emulate the curvature on the natural profile.

Model solutions can attain quite good agreement with the natural data using this method (Figure 13). Slight deviations near the core may suggest a degree of two-step history, with some degree of diffusion prior to surface emplacement, though to explicitly fit this is hard to justify. Scenarios involving the departure of an individual crystal from the single cooling trend for a period of time are not difficult to imagine in nature, yet we adhere to the cooling and growth rates expected from the system scale observations summarised by the model (Figure 7).

Extension to the broader Piton de la Fournaise dataset. Using the dynamic methods, we re-modelled 13 profiles from the RU0701 dataset. We selected profiles that exhibited a poor fit when initially modelled at a single temperature of 1126ºC and fixed boundary condition.

By incorporating a cooling rate and a growth rate guided by the expected behaviour of the cooling magma (Figure 7) the model produced results that are in good agreement with the natural profiles. Six of these profiles from two crystals (RU0701_2_G and RU0701_2_I) are shown in Figure 14. The remaining six remodelled profiles are included in Supplementary Data A. All of the remodelled profiles are consistent with an average cooling rate of -0.5 ºC/hr (±0.1 ºC) and an average growth rate of $\sim 1.9 \times 10^{-11}$ ms^{-1}, over the cooling range 1127-967ºC. These models translate to new diffusion timescales of, on average, 13 days (with a minimum timescale of 10 days, and a maximum timescale of 17 days).

511 The textural evidence, profile shapes at the crystal rims and short diffusion timescales
512 indicate that the diffusion rims are late-stage, and most likely related to lava flow cooling. As an
513 external check on the viability of our re-modelled timescales, we would expect the lava flow
514 cooling time and the re-modelled diffusion timescales to be similar. We can use the following
515 equation to calculate the cooling time of the lava flow;

516 $$T = \frac{A^2}{\pi^2\ K} \qquad (2)$$

517 Where T is the time in seconds, A is the thickness of the lava flow in meters, and K is the
518 thermal diffusivity of a basalt (Hon et al., 1994). This simple lava flow cooling rate calculation
519 (with a lava flow thickness of 2-3 m) gives cooling rates of 9-19 days. The independent line of
520 cooling rate calculation agrees with the re-modelled diffusion timescales using the models that
521 incorporate cooling rate (and thereby changing boundary condition) and crystal growth rate, and
522 so lends confidence to our approach.

523

524 **Advanced Discussion**

525 It is reasonable to consider that the diffusion 'clock' in each crystal can be set at different times
526 yet stop at effectively the same time (on eruption). Scatter within crystals due to natural
527 variation, which if understood and placed into broader petrological context, can lead to detailed
528 understanding of magmatic and/or volcanic phenomena (e.g. Pankhurst et al. 2018b). Diffusion
529 timescale scatter between crystals could, however, also occur even if diffusion clocks are set
530 simultaneously if complicating factors such as proximity to other crystals, exposure to different
531 melts, mineral grains or vesicles blocking diffusion have persisted for a significant fraction of
532 time *and* if simplistic modeling is applied. Scatter within individual crystals could reflect

limitations on the quality of modeling and/or be due to real complications such as crystal growth, changing boundary conditions, sectioning effects and 3D crystal geometry.

Shallow sectioning effects

There is limited control for ideal alignment of crystals during the preparation of grain mounts, and effectively no control in the case of thin sections. But in contrast to the expected bias towards shallow angles (Pearce, 1984), our dataset largely consists of boundaries with relatively small deviations (<10°) from being ideally sectioned. As a consequence, accounting for the measured sectioning angle, has a relatively limited effect of reducing the timescales from mostly 7-45 days (outliers between 60-104 days) to 6-44 days (outliers between 62-82 days; Figure 15).

Since the combined uncertainty of binary Fe-Mg inter-diffusion in olivine due to temperature, activation energy and D_0 is 0.34-0.38 log units, an average 0.011 log shift towards longer timescales cannot be considered critical at a population level, for olivine grains of this large size relative to their narrow diffusion width.

Overall, the relatively low occurrence of significantly shallow sectioning angles within the RU0701 dataset is likely due to the subconscious selection of crystal slices and faces analysed combined with the large relative difference in crystal size to profile length. Even when trying to remove bias, unworkable crystal slices do not make the initial selection. Sectioning angle uncertainty is likely to become more important in small datasets, and in circumstances where context is lacking or where only one crystal margin can be considered.

Understanding crystal shape

555 Shea et al. (2015a) conducted a comparison between 1D, 2D and 3D diffusion modeling of
556 timescales from slices based on theoretical polyhedral, spherical and cuboid shapes. They found
557 that timescale distributions vary depending on the crystal faces present and the angles between
558 the faces. These authors also showed that the difference between measured/calculated to real
559 timescales can be especially variable where diffusion fronts from adjacent crystal faces converge
560 i.e. where profiles are extracted nearer corners. This results in a longer apparent profile and
561 therefore an apparent longer timescale when modelled. These zones are a common feature of
562 polyhedral crystal slices (a common natural crystal shape) where faces meet at <180º.

563 We considered the Piton crystal form, as rounding of crystal faces will enhance the effect
564 of merging diffusion fronts, and the arrangement of crystals. We also considered if grains were
565 single crystals or present as aggregates and these came together, whether by syneusis
566 (Schwindinger and Anderson, 1989) or paired nucleation. Diffusion timescales may be affected
567 by a 'pre-history' of individual parts, a change in boundary conditions that coincide with their
568 coming together.

569 An observation made possible here due to the 3D data is the absence of an (001) face; the
570 theoretical olivine shape used in the study of Shea et al. (2015a) does have an (001) face.
571 Furthermore, the 3D data demonstrate that the olivine crystals do not conform to an 'ideal'
572 solitary crystal morphology. An initial comparison of a slice through the polyhedral olivine
573 shape used by Shea et al. (2015a) and a slice through a 3D rendered natural crystal at the same
574 orientation is sufficient to illustrate that the natural crystal is not perfectly euhedral and that
575 additional faces are present within crystals (Figure 16). In this case, a timescale calculation is
576 unlikely to suffer much uncertainty due to the relatively narrow margins and wide areas from
577 which to choose a profile away from corners. But without 3D data, this view would only be

intersected by chance, and in the cases of smaller crystals with broader margins even subtle departures from an ideal shape will magnify the geometric uncertainties when studying natural crystals. Further work, and more comprehensive natural 3D data, is required to better link the value gained from using generalised synthetic crystal shapes with applications across a variety of settings.

The XMT dataset shows that natural crystals have added morphological complexity that may interact with diffused zones to a greater extent than has been considered in previous studies where only idealised morphologies have been investigated. It is clear that the effects of euhedrality and arrangement of the crystal agglomerates need to be more fully quantified to understand how crystal shape uncertainties may affect calculated diffusion timescales. Uncertainty on calculated diffusion timescales would likely increase yet placing 'hard' numbers on this effect is difficult to establish since we used a polychromatic beam prior to method developments that attempt to address the inherent problems in deriving quantitative attenuation data using polychromatic beams (Pankhurst et al., 2014; Pankhurst et al., 2018b; Pankhurst et al., 2018c).

Fully quantitative 3D composition data throughout olivine crystals, which at this stage of research is still only possible using a monochromatic X-ray beams, is needed to address these questions. Current work strives to develop a 3D method that uses polychromatic beams, is rapid, chemically quantitative *and* able to resolve high frequency gradients such as in crystal margins, with the same confidence as 2D imaging. At present, the 3D data provides the important observations that this natural crystal population is strongly affected by crystal rounding and are mostly present as crystal agglomerates.

601 **Simultaneous crystal growth and changing boundary conditions**

602 Each of the 13 dynamically-modelled profiles were remodelled with a global cooling
603 rate, and as the magma cools, the boundary condition is continuously shifting, with simultaneous
604 crystal growth. The cooling rate used for each profile (-0.5 ±0.1°C/hr) is consistent with
605 diffusion related to quench and lava flow cooling and inferred from textural observations (an
606 average peak growth rate of ~1.9×10^{-11} ms^{-1} was applied to each profile). Most profiles (11 of
607 13 profiles) were remodelled using an accelerating growth rate, rather than a linear growth rate,
608 as the growth rate seems also to be a function of temperature and has to be increasing with
609 continued cooling in most cases, based on the profile shapes.

610 Although the profiles show an apparent increased diffusion length due to crystal growth
611 and changing boundary conditions effects, our advanced models accommodate how diffusion
612 speed slows as the lava flow cools, and so the diffusion timescales do not become significantly
613 shorter nor is the scatter of the dataset significantly reduced. As a result of reducing epistemic
614 uncertainty there is an attendant increase in confidence that the scatter reflects real variation in
615 crystal histories. This is corroborated by the observation of different final rim compositions
616 (between Fo_{72} and Fo_{60}): even though the crystals reflect a common cooling environment, the
617 details of their final experiences were controlled locally by the availability of melt and other
618 considerations including pore space. This appears to be particularly important in the case of
619 samples from lava flows where post-eruption cooling must be considered in petrogenetic
620 interpretations, which could, in turn, free models of deeper magmatic plumbing system structure
621 and dynamics from this frequently observed complexity. Cheng et al. (2020) suggest that it can
622 be possible to create simple diffusion curves (as seen within our samples) as a result of changing
623 boundary conditions due to flow dynamics, if there is sufficient residence time for complex

zoning patterns to evolve into simple zoning – we do not consider this to be the case for these PdlF olivines.

Implications

Uncertainty of individual diffusion timescales can be considerably reduced using a combination of three-dimensional observation and dynamic forward modeling that includes an assessment of growth and changing boundary conditions. The quantification of the sources of uncertainty upon the RU0701 dataset allows us to better understand how they, and by extension their corrections, affect timescale distributions and interpretation. The results have implications for the design of crystal diffusion studies which we recommend should explicitly consider sectioning angle, 3D geometries, crystal growth or changing boundary condition corrections on reported timescales. A re-appraisal of modeling assumptions, as demonstrated here, may significantly improve both the quality and quantity of data recovered from a suite of crystals. It follows that increased dataset size per investment in resources as well as increased confidence in timescale outputs will have value as kinetic and kinematic views of magmatic processes improve towards full physical history reconstruction (e.g. Pankhurst et al., 2018b).

Our case study demonstrates that agreement can be found between the timescales of cooling at the scale of a lava flow and the range exhibited by the individual crystals it contains. This result would not have been possible without the need to consider dynamic modeling as a solution to poorly-fitting initial profiles to simplistic diffusion models. The system-scale information required, such as intensive parameters and a model of melt evolution with cooling in turn provide a framework to better contextualise the variations observed in final rim composition and timescales. The consistently high-quality fits between raw data and models using a common

cooling history and growth rate leads us to frame new questions regarding the variation of rim compositions and other details which will be addressed in a subsequent contribution. It also provides a demonstration that the cooling regime within a lava flow can be obtained on the crystal scale, which likely holds value in understanding more complex flow settings.

The value in improving the quality of diffusion timescale datasets is expected to provide a better return on data-gathering investment, including observations at the population scale that are based on larger and more complete datasets and increase the detail and therefore utility of interpretations.

Acknowledgements

We would like to thank the reviewers and editor for their constructive comments and handling of the manuscript. We thank Thomas Shea for the helpful discussions and use of the theoretical olivine shape MATLAB code. John Wynn Williams and Richard Walshaw are thanked for their assistance with sample preparation and the analytical facilities at the University of Leeds. Roger Clark and Adam Booth are thanked for providing valuable writing time to enable the preparation of this work for publication. Lois Courtois and Sara Nonni are thanked for assistance with XMT scanning.

Funding

FKC and DJM acknowledge NERC Studentship number 1367441 for supporting this work. MJP acknowledges an AXA Research Fund Fellowship which supported part of this work. Sample

collection was made possible by the National Geographic Society (NGS 8330-07). XMT scanning was funded through UK-NERC grants NE/M013561/1 and NE/N018575/1.

References

Albarède, F., Luais, B. and Fitton, G. (1997) The geochemical regimes of Piton de la Fournaise volcano (Réunion) during the last 530 000 years. Journal of Petrology, 38(2), 171–201.

Allan, A. S. R., Morgan, D. J., Wilson, C. J. N. and Millet, M. A. (2013) From mush to eruption in centuries: Assembly of the super-sized Oruanui magma body. Contributions to Mineralogy and Petrology, 166(1), 143–164.

Arganda-Carreras, I., Kaynig, V., Rueden, C., Eliceiri, K. W., Schindelin, J., Cardona, A. and Seung, H. S. (2017) Trainable weka segmentation: a machine learning tool for microscopy pixel classification. Bioinformatics, 33, 2424-2426.

Ariskin, A. A., Frenkel, M. Y., Barmina, G. S., Nielsen, R. L. (1993) COGMAGMAT: A fortran program to model magma differentiation processes. Computers & Geosciences, 19, 115-1170

Asimow, P. D. and Ghiorso, M. S. (1998) Algorithmic Modifications Extending MELTS to Calculate Subsolidus Phase Relations. American Mineralogist, 83, 1127–1131.

Beattie, P. (1993) Olivine-melt and orthopyroxene-melt equilibria. Contributions to Mineralogy and Petrology, 115, 103-111

Blundy, J. and Cashman, K. (2008) Petrologic Reconstruction of Magmatic System Variables and Processes. Reviews in Mineralogy and Geochemistry, 69(1), 179–239.

Boivin, P. and Bachèlery, P. (2009) Petrology of 1977 to 1998 eruptions of Piton de la

690 Fournaise, La Réunion Island. Journal of Volcanology and Geothermal Research, 184(1–2),
691 109–125.

692 Bouvet de Maisonneuve, C., Costa, F., Huber, C., Vonlanthen, P., Bachmann, O. and Dungan,
693 M. A. (2016) How do olivines record magmatic events? Insights from major and trace element
694 zoning. Contributions to Mineralogy and Petrology, 171(6), 1–20.

695 Boyd, F. R. and Mertzman, S. A. (1987) Composition and structure of the Kaapvaal lithosphere,
696 southern Africa. Magmatic Processes - Physiochemical Principles. In Geochemical Society
697 Special Publications, p. 13-24. Geochemical Society Special Publication.

698 Brady, J. B. and Cherniak, D. J. (2010) Diffusion in Minerals: An Overview of Published
699 Experimental Diffusion Data. Reviews in Mineralogy and Geochemistry, 72(1), 899–920.

700 Breiman, L. (2001) Random Forests. Machine Learning, 1–33.

701 Buades, A., Coll, B. and Morel, J.-M. (2011) Non-Local Means Denoising. Image Processing
702 Online.

703 Buening, D. K. and Buseck, P. R. (1973) Fe-Mg lattice diffusion in olivine. Journal of
704 Geophysical Research, 78(29), 6852–6862.

705 Bureau, H., Pineau, F., Métrich, N., Semet, M. and Javoy, M. (1998) A melt and fluid inclusion
706 study of the gas phase at Piton de la Fournaise volcano (Réunion Island). Chemical geology, 147,
707 115-130.

708 Chakraborty, S. (2010) Diffusion Coefficients in Olivine, Wadsleyite and Ringwoodite. Reviews
709 in Mineralogy and Geochemistry, 72(1), 603–639.

710 Chakraborty, S., Farver, J. R., Yund, R. A. and Rubie, D. C. (1994) Mg tracer diffusion in
711 synthetic forsterite and san carlos olivine as a function of P, T and fO2. Physics and Chemistry

712 of Minerals, 21, 489–500.

713 Charlier, B. L. A., Morgan, D. J., Wilson, C. J. N., Wooden, J. L., Allan, A. S. R. and Baker, J.
714 A. (2012) Lithium concentration gradients in feldspar and quartz record the final minutes of
715 magma ascent in an explosive supereruption. Earth and Planetary Science Letters, 319–320,
716 218–227.

717 Cheng, L., Costa, F. & Bergantz, G. (2020). Linking fluid dynamics and olivine crystal scale
718 zoning during simulated magma instrusion. Contributions to Mineralogy and Petrology, 175: 53

719 Clague, D. A. and Denlinger, R. P. (1994) Role of olivine cumulates in destabilizing the flanks
720 of Hawaiian volcanoes. Bulletin of Volcanology, 56(6–7), 425–434.

721 Costa, F. and Morgan, D. (2010) Time Constraints from Chemical Equilibration in Magmatic
722 Crystals. In Dosseto, A., Turner, S. P., and Van Orman, J. A. (eds) Timescales of Magmatic
723 Processes: From Core to Atmosphere, 1st edition, p. 125-129. Blackwell Publishing Ltd.

724 Costa, F. and Chakraborty, S. (2004) Decadal time gaps between mafic intrusion and silicic
725 eruption obtained from chemical zoning patterns in olivine. Earth and Planetary Science Letters,
726 227(3–4), 517–530.

727 Costa, F., Chakraborty, S. and Dohmen, R. (2003) Diffusion coupling between trace and major
728 elements and a model for calculation of magma residence times using plagioclase. Geochemica
729 et Cosmochimica Acta, 67(12), 2189–2200.

730 Costa, F., Dohmen, R. and Chakraborty, S. (2008) Time Scales of Magmatic Processes from
731 Modeling the Zoning Patterns of Crystals. Reviews in Mineralogy and Geochemistry, 69(1),
732 545–594.

733 Costa, F. and Dungan, M. (2005) Short time scales of magmatic assimilation from diffusion

734 modeling of multiple elements in olivine. Geology, 33(10), 837.

735 Couperthwaite, F. K., Thordarson, T., Morgan, D. J., Harvey, J., Wilson, M. (2020) Diffusion
736 timescales of magmatic processes in the Moinui lava eruption at Mauna Loa, Hawai'i, as inferred
737 from bimodal olivine populations. Journal of Petrology. Accepted June 2020.

738 Danyushevsky, L. V. (2001) The effects of small amounts of H_2O on crystallisation of mid-
739 ocean ridge and backarc basin magmas. Journal of Volcanology and Geothermal Research, 110,
740 265-280

741 Danyushevsky, L. V. and Plechov, P. (2011) Petrolog3: Integrated software for modeling
742 crystallization processes. Geochemistry, Geophysics, Geosystems, 12(7).

743 Darbon, J., Cunha, D., Chan, T. F., Osher, S. and Jensen, G. J. (2008) Fast nonlocal filtering
744 applied to electron cryomicroscopy. In Proceedings of the 5th IEEE International Symposium on
745 Biomedical Imaging: From Nano to Macro, 1331–1334.

746 Dohmen, R., Becker, H.-W. and Chakraborty, S. (2007) Fe–Mg diffusion in olivine I:
747 experimental determination between 700 and 1,200°C as a function of composition, crystal
748 orientation and oxygen fugacity. Physics and Chemistry of Minerals, 34(6), 389–407.

749 Dohmen, R. and Chakraborty, S. (2007a) Fe–Mg diffusion in olivine II: point defect chemistry,
750 change of diffusion mechanisms and a model for calculation of diffusion coefficients in natural
751 olivine. Physics and Chemistry of Minerals, 34(6), 409–430.

752 Dohmen, R. and Chakraborty, S. (2007b) Fe–Mg diffusion in olivine II: point defect chemistry,
753 change of diffusion mechanisms and a model for calculation of diffusion coefficients in natural
754 olivine. Erratum to Physics and Chemistry of Minerals, 34(6), 409–430.

755 Dohmen, R. and Milke, R. (2010) Diffusion in Polycrystalline Materials: Grain Boundaries,

Mathematical Models, and Experimental Data. Reviews in Mineralogy and Geochemistry, 72(1), 921–970.

Donovan, J., Kremser, D. and Fournelle, J. (2012) Probe for EPMA: Acquisition automation and analysis. Probe Software Inc.

Famin, V., Welsch, B., Okumura, S., Bachèlery, P. and Nakashima, S. (2009) Three differentiation stages of a single magma at Piton de la Fournaise volcano (Reunion hot spot). Geochemistry, Geophysics, Geosystems, 10(1), Q01007

Furi, E., Hilton, D. R., Murton, B. J., Hémond, C., Dyment, J. and Day, J. M. D. (2011) Helium isotope variations between Réunion Island and the Central Indian Ridge (17-21 S): New evidence for ridge-hotspot interaction. Journal of Geophysical Reearch: Solid Earth, 116(B2)

Geiger, H., Mattson, T., Deegan, F, M., Troll, V. R., Burchardt, S., Gudmundsson, O., Tryggvason, A., Krumbholz, M. and Harris, C. (2016) Magma plumbing for the 2014-2015 Holuhrun eruption, Iceland. Geochemistry Geophysics Geosystems, 17, 2825–2834.

Ghiorso, M. S. and Sack, R. O. (1995) Chemical Mass Transfer in Magmatic Processes. IV. A Revised and Internally Consistent Thermodynamic Model for the Interpolation and Extrapolation fo Liquid-Solid Equilibria in Magmatic Systems at Elevated Temperatures and Pressures. Contribution to Mineralogy and Petrology, 119, 197–212.

Hartley, M. E., Morgan, D. J., Maclennan, J., Edmonds, M. and Thordarson, T. (2016) Tracking timescales of short-term precursors to large basaltic fissure eruptions through Fe–Mg diffusion in olivine. Earth and Planetary Science Letters, 439, 58–70.

Hastie, T., Tibshirani, R. and Friedman, J. (2008) The Elements of Statistical Learning: Data Mining, Inference and Prediction. Second edition. Springer.

778 Helz, R. T. and Thornber, C. R. (1987) Geothermometry of Kilauea Iki lava lake, Hawaii.
779 Bulletin of Volcanology, 651–668.

780 Hon, K., Kauahikaua, J., Denlinguer, R. and Mackay, K. (1994) Emplacement and inflation of
781 pahoehoe sheet flows: Observations and measurements of active lava flows on Kilauea Volcano,
782 Hawaii. Geological Society of America Bulletin, 106(3), 351–370.

783 Huebner, J. and Sato, M. (1970) The oxygen fugacity-temperature relationships of manganese
784 oxide and nickel oxide buffers. American Mineralogist, 55, 934–952.

785 Jarosewich, E. Nalen, J. A. & Norberg, J. A. (1980) Reference standards for electron microprobe
786 analysis. Geostandards Newsletter, 4, 43-47.

787 Jerram, D.A., Dobson, K. J., Morgan, D. J. & Pankhurst, M. J. (2018) The petrogenesis of
788 magmatic systems: using igneous textures to understand magmatic processes. Volcanic and
789 Igneous Plumbing Systems. Elsevier Inc.

790 Kahl, M., Chakraborty, S., Costa, F., Pompilio, M. (2011) Dynamic plumbing system beneath
791 volcanoes revealed by kinetic modeling and the connection to monitoring data: an exmaple from
792 Mt. Etna. Earth and Planetary Science Letters, 308, 11-22

793 Kahl, M., Chakraborty, S., Costa, F., Pompilio, M., Liuzzo, M. and Viccaro, M. (2013)
794 Compositionally zoned crystals and real-time degassing data reveal changes in magma transfer
795 dynamics during the 2006 summit eruptive episodes of Mt. Etna. Bulletin of Volcanology, 75(2),
796 692.

797 Kile, D. (2009) The universal stage: The past, present, and future of a mineralogical research
798 instrument. Geochemical News, 1–21.

799 Lénat, J.-F., Bachèlery, P. and Merle, O. (2012) Anatomy of Piton de la Fournaise volcano (La

Réunion, Indian Ocean). Bulletin of Volcanology, 74(9), 1945–1961.

Lesher, C. E. (2010) Self-diffusion in Silicate Melts: Theory, Observations and Applications to Magmatic Systems. Reviews in Mineralogy and Geochemistry, 72(1), 269–309.

Lloyd, G. E. (1987) Atomic Number and Crystallographic Contrast Images with the SEM: A Review of Backscattered Electron Techniques. Mineralogical Magazine, 51(359), 3–19.

Longpré, M.-A., Staudacher, T. and Stix, J. (2006) The November 2002 eruption at Piton de la Fournaise volcano, La Réunion Island: ground deformation, seismicity, and pit crater collapse. Bulletin of Volcanology, 69(5), 511–525.

Lynn, K. J., Garcia, M. O., Shea, T., Costa, F. and Swanson, D. A. (2017) Timescales of mixing and storage for Keanakāko‘i Tephra magmas (1500–1820 C.E.), Kīlauea Volcano, Hawai‘i. Contributions to Mineralogy and Petrology, 172(9).

Martin, V. M., Morgan, D. J., Jerram, D. a, Caddick, M. J., Prior, D. J. and Davidson, J. P. (2008) Bang! Month-scale eruption triggering at Santorini volcano. Science, 321(5893), 1178.

Morgan, D. J., Blake, S., Rogers, N. W., De Vivo, B., Rolandi, G. and Davidson, J. P. (2006) Magma chamber recharge at Vesuvius in the century prior to the eruption of A.D. 79. Geology, 34(10), 845.

Morgan, G. B. V. and London, D. (1996) Optimizing the electron microprobe analysis of hydrous alkali aluminosilicate glasses. American Mineralogist, 81, 1176–1185.

Pankhurst, M. J., Dobson, K. J., Morgan, D. J., Loughlin, S. C., Thordarson, T., Lee, P. D. and Courtois, L. (2014) Monitoring the magmas fuelling volcanic eruptions in near-real-time using x-ray micro-computed tomography. Journal of Petrology, 55, 671-684.

Pankhurst, M. J., Walshaw, R. and Morgan, D. J. (2016) Major element chemical heterogeneity

in Geo2 olivine microbeam reference material: a spacial approach to quantifying heterogeneity in primary reference materials. Geostandards and Geoanalytical Research, 41, 85-91

Pankhurst, M. J., Fowler, R., Courtois, L., Nonni, S., Zuddas, F., Atwood, R. C., Davis, G. R. and Lee, P. D. (2018a) Enabling three-dimensional densitometric measurements using laboratory source X-ray micro-computed tomography. SoftwareX, 7, 115–121.

Pankhurst, M. J., Morgan, D. J., Thordarson, T. and Loughlin, S. C. (2018b) Magmatic crystal records in time, space, and process, causatively linked with volcanic unrest. Earth and Planetary Science Letters, 493, 231–241.

Pankhurst, M. J., Vo, N. T., Butcher, A. R., Long, H., Wang, H., Nonni, S., Harvey, J., Gudfinnsson, G., Fowler, R., Atwood, R., Walshaw, R., Lee, P. (2018c) Quantitative measurement of olivine composition in three dimensions using helical-scan X-ray-microtomography. American Mineralogist, 103 (11), 1800-1811.

Pearce, T. H. (1984) The analysis of zoning in magmatic crystals with emphasis on olivine. Contributions to Mineralogy and Petrology, 86(2), 149–154.

Peltier, A., Bachèlery, P. and Staudacher, T. (2009) Magma transport and storage at Piton de La Fournaise (La Réunion) between 1972 and 2007: A review of geophysical and geochemical data. Journal of Volcanology and Geothermal Research, 184(1–2), 93–108.

Peters, B. J., Day, J. M. D. and Taylor, L. A. (2016) Early mantle heterogeneities in the Reunion hotspot source inferred from highly siderophile elements in cumulate xenoliths. Earth and Planetary Science Letters, 448, 150–160.

Petrone, C. M., Braschi, E., Francalanci, L., Casalini, M., Tommasini, S. (2018) Rapid micing and short storage timescale in the magma dynamics of a steady-state volcano, 492, 206-221

844 Putirka, K. D. (2008) Thermometers and Barometers for Volcanic Systems. Reviews in
845 Mineralogy and Geochemistry, 69(1), 61–120.

846 Reed, S. J. B. (2005) Electron Microprobe Analysis and Scanning Electron Microscopy in
847 Geology. Second Edition. Cambridge University Press.

848 Rhodes, J. M. and Vollinger, M. J. (2005) Ferric/ferrous ratios in 1984 Mauna Loa lavas: a
849 contribution to understanding the oxidation state of Hawaiian magmas. Contributions to
850 Mineralogy and Petrology, 149(6), 666–674

851 Ruth, D. C. S., Costa F., Bouvet de Maisonneve, C., Franco, L., Cortés and Calder, E. S. (2018)
852 Crystal melt inclusion timescales reveal the evolution of magma migration before eruption.
853 Nature Communications, 9, 2657

854 Schneider, C. A., Rasband, W. S. and Eliceiri, K. W. (2012) NIH Image to ImageJ: 25 years of
855 image analysis. Nature Methods. Nature Publishing Group, 9(7), 671–675.

856 Schwindinger, K. R. and Anderson, A. T. (1989) Synneusis of Kilauea Iki olivines.
857 Contributions to Mineralogy and Petrology, 103(2), 187–198.

858 Shea, T., Costa, F., Krimer, D. and Hammer, J. E. (2015a) Accuracy of timescales retrieved from
859 diffusion modeling in olivine: A 3D perspective. American Mineralogist, 100(10), 2026–2042.

860 Shea, T., Lynn, K. J. and Garcia, M. O. (2015b) Cracking the olivine zoning code:
861 Distinguishing between crystal growth and diffusion. Geology, 43(10), 935–938.

862 Soille, P. and Vincent, M. (1990) Determining watersheds in digital pictures via flooding
863 simulations. Society of Photo-Optical Instrumentation Engineers, Proceedings Volume 1360,
864 240–250.

865 Wagstaff, K., Cardie, C., Rogers, S. and Schroedl, S. (2001) Constrained K-means clustering

with background knowledge. Proceedings of the Eighteenth International Conference on Machine Learning, 577–584.

Wieser, P.E., Vukmanovic, Z., Kilian, R., Ringe, E., Holness, M. B., Maclennan, J. and Edmonds, M. (2019) To sink, swim, twin or nucleate: A critical appraisal of crystal aggregation processes. Geology, 47, 948-952

Welsch, B., Faure, F., Famin, V., Baronnet and Bachelery, P. (2013) Dendritic Crystallization: A Single Process for all the Textures of Olivine in Basalts?. Journal of Petrology, 54(3), 539–574.

Figure Captions

Figure 1. A frequently encountered limitation of simple ionic diffusion modelling applied to natural crystals. (**a**) Schematic showing relaxation of an initial chemical disequilibria profile (blue) as a function of time (t1-3) within one phase, by diffusion (black lines). Any interaction with external boundaries will result in a change of profile shape. Any change in thermal condition through time will result in an error in calculated duration should a constant temperature be assumed (**b**) Example of a compositional profile (RU0701_3_G4) extracted from a zoned crystal (**c**) The best-fit simple diffusion model (red) does not match the measured profile nearer the core due to enhanced curvature of the profile (i) nor at the crystal rim (ii) due to an inversion point in the profile gradient. Due to these poor fits, this crystal would traditionally no longer be considered for inclusion in a timescale database. Poor-fitting profiles represent an important source of potential bias

888 Figure 2. Location map of the 2002 lava flow at Piton de la Fournaise using GeoMapp App. A
889 red star indicates the vents location and the central caldera and progressive collapse structures
890 are indicated by the annotations and map shading as per Longpre et al. (2007) and Servadio et al.
891 (2013).

892

893 Figure 3. BSE images representing the range of crystal textures observed in this study. (**a**) A
894 large, euhedral olivine (ol) agglomerate with homogeneous BSE response except for relatively
895 narrow zonation at the edges and surrounded by a microlitic groundmass (**b**) microlitic
896 groundmass containing olivine (ol), plagioclase (plag), clinopyroxene (cpx) and oxides (ox). (**c**)
897 a smaller, olivine crystal, or section through a large crystals' terminus exhibits broadly zoned
898 margin, and also surrounded by microlitic groundmass (**d**) the rim of a large, euhedral olivine
899 showing a narrow, diffused zone

900

901 Figure 4. Scatter amongst calculated diffusion timescales is observed both within a single crystal
902 and between crystals (n = 30). All timescales are calculated using AUTODIFF and are corrected
903 for anisotropy. The average uncertainty is 0.38 log units (1σ). If all results corrected to a single
904 timescale that has geological meaning – a common hypothesis – all bars would be of equal
905 height. Black dashed lines separate crystals from different thin sections.

906

907 Figure 5. Schematic diagram adapted from Costa & Morgan (2010) illustrating the effects of
908 shallow sectioning (thick horizontal black line is sectioning plane) of a chemically zoned crystal
909 (concentric rectangles). The part of the crystal to the left will display a stretch effect three times

910 the true length of the gradient that diffusion is acting across. The part of the crystal to the right
911 has also been stretched but to a lesser extent. The narrowest profiles that also are at a maximum
912 distance from corners and as such are at least affected by are indicated by red arrows. Arrow (i)
913 serves to illustrate that the boundary conditions affecting the measured profile are not captured
914 by the 2D plane of the section; these are lost to the saw and grinder. Arrow (ii) serves to illustrate
915 the proximity to a corner that can amplify out-of-plane effects on measured profiles.

916

917 Figure 6. The percentage area of an olivine manually segmented from raw, XMT images
918 compared with the percentage area of olivine segmented from these using 'k-means
919 cluster'(green), watershed (blue) and trainable weka (red) segmentation methods. There are ten
920 data points for each method, each from one slice evenly spaced throughout the stack of images
921 comprising the segmented olivine. The high r^2 value indicates that the image analysis techniques
922 are acceptable to apply to slices between those manually segmented, and so are able to efficiently
923 generate 3D binary stacks of "olivine" and "not olivine" and reveal 3D crystal shapes.

924

925 Figure 7. Evolution of olivine equilibrium composition over the temperature range 1250ºC-
926 950ºC modeled using Petrolog3. The modeling conditions used are as follows; olivine-melt
927 equilibria (Beattie, 1993), plagioclase-melt equilibria (Danyshevsky 2001), clinopyroxene-melt
928 equilibria (Danyshevsky 2001), opx-melt equilibria (Beattie, 1993), magnetite-melt equilibria
929 (Ariskin et al., 1993). Pressure and buffers; at 2 kilobar, QFM buffer, at 1 atmosphere, QFM+2.
930 Calculation step; 0.01% crystallisation.

931

Figure 8. Flow chart of the 1-dimensional dynamic diffusion models.

Figure 9. The frequency of angles measured using a Universal Stage (U-Stage) between crystal boundary and the plane normal to the sectioning plane. Each data point (n = 104) is a measurement from where a diffusion profile was extracted. The red lines bracket points that would require a correction of < 10% and <20% due to shallow sectioning effects.

Figure 10. Composite images of four olivine clusters digitally segmented from the XMT data using '*Image J*' and *AVISO*. Each cluster (**a**)-(**d**) is shown from 4 different orientations. (**e**) An 'idealised' theoretical olivine crystal used in various studies e.g. Shea et al. (2015a) compared against an olivine cluster imaged using XMT. Miller indices denote matching faces and black lines highlight crystal face edges. The (001) face is not present in any of the Piton de la Fournaise olivine, and it is rare that olivine exists as solitary crystals.

Figure 11. Sequence of diffusion curves generated using the dynamic modeling code investigates different cooling rates. A series of cooling rates were applied to generate a changing boundary condition within the model over the cooling range 1127-967°C. No crystal growth is incorporated into these curves. A natural olivine diffusion profile (RU0701_A_1) is overlain in black (labelled "measured'). The dynamic models show a poor fit to the raw crystal data; the natural profile does not result from varying the cooling rate in isolation.

Figure 12. Sequence of diffusion curves generated using the dynamic modeling code investigating changing growth rate. A series of crystal growth rates were applied within the model. The boundary condition is fixed at a single value. A natural olivine diffusion profile (RU0701_A_1) is overlain in black. The dynamic models show a poor fit to the raw crystal data; the natural profile does not result from varying the growth rate in isolation.

Figure 13. An example of how using the dynamic modeling code and adjusting the parameters of cooling rate and growth rate can return a good fit between the model and the natural crystal data (RU0701_1_A1). The 13 re-modelled profiles (including this one) are consistent with an average cooling rate of -0.5 °C/hr (+/- 0.1 °C/hr) and an average growth rate of ~1.9 x 10^{-11} ms^{-1}, over the cooling range 1127-967 °C. The diffusion timescale for this dynamically modeled profile is 12 days, reduced from 20 days.

Figure 14. Applying the dynamic diffusion modeling code and adjusting the parameters of cooling rate and growth rate shows we can acquire a good fit between the model and the natural crystal data across many profiles of the PdlF dataset. We show a further 6 of the 13 re modeled profiles above. The initial diffusion timescales ranged from 11-31 days. Dynamically modeled profiles shown here were each fit using a global cooling rate (-0.5 °C/hr (+/-0.1°C)) and an average peak growth rate of ~1.9 x 10^{-11} ms^{-1}. The diffusion timescales reduce to 11-17 days.

Figure 15. Comparison between timescales calculated with and without measured sectioning angle by U-stage. Note: these timescale shifts do not consider the effects of a shift in diffusivity.

975 (**a**) timescales uncorrected for shallow sectioning with the population of timescales ranging from
976 7-45 days with outliers between 60-104 days (**b**) timescales corrected for shallow sectioning with
977 a population of timescales ranging from 6-44 days with outliers between 62-82 days. The
978 corrected timescales show an overall shortening compared to the corrected timescales.

979

980 Figure 16. A comparison of (**a**) a slice through a synthetic olivine crystal generated using olivine
981 shape matlab code from Shea et al. (2015a) and (**b**) slice through a natural Piton de la Fournaise
982 crystal (from an SEM backscattered electron image) at the same orientation. Red ellipses
983 highlight extra faces that are present in the synthetic crystal but not in the natural crystal, and the
984 red and yellow lines in (b) highlight where two crystal faces are present in the natural crystal,
985 whereas only one is present in the synthetic. The natural crystal also has embayments. (**c**) an
986 olivine imaged in 3D and segmented from the groundmass using *Image J* and *AVISO*.

987
988
989
990
991
992
993
994

Figure 1

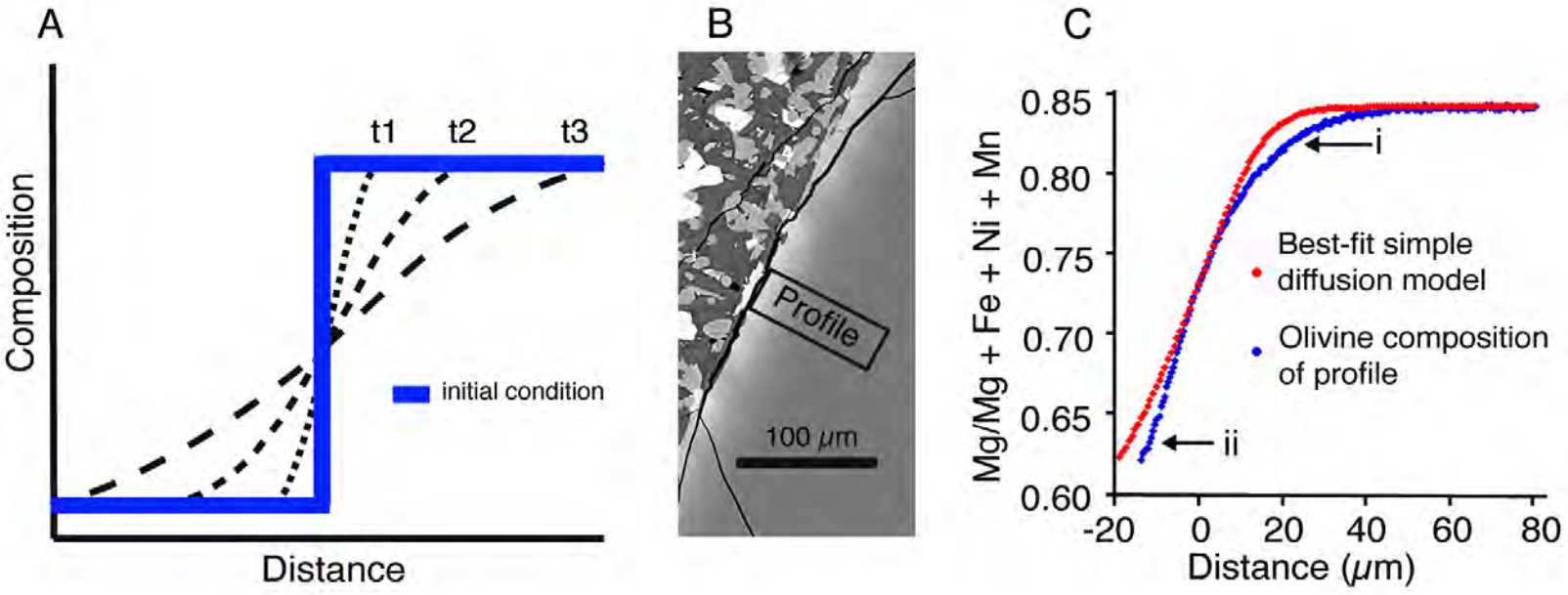
A
t1
t2
t3
Composition
initial condition
Distance
B
Profile
100 μm
C
0.85
0.80
0.75
0.70
0.65
0.60
Mg/Mg + Fe + Ni + Mn
i
ii
Best-fit simple diffusion model
Olivine composition of profile
-20
0
20
40
60
80
Distance (μm)

Figure 2

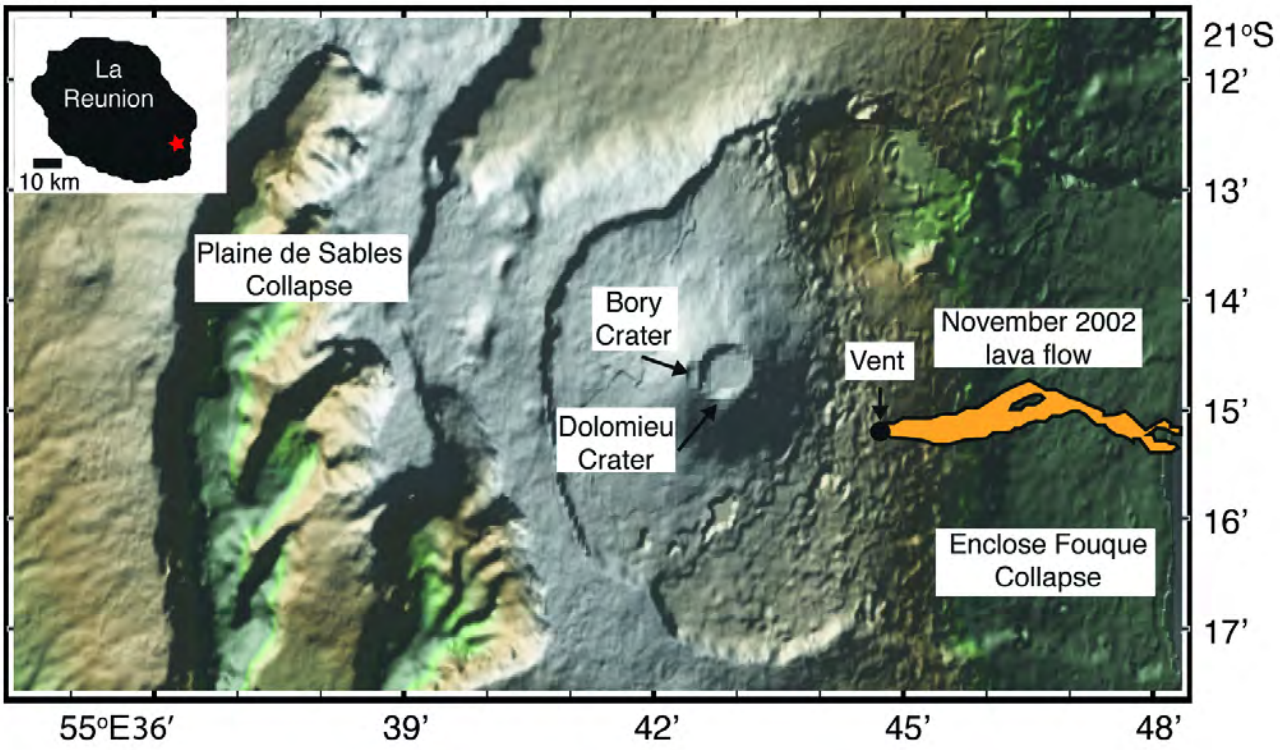
La Reunion
10 km
Plaine de Sables Collapse
Bory Crater
Dolomieu Crater
Vent
November 2002 lava flow
Enclose Fouque Collapse
21°S
12'
13'
14'
15'
16'
17'
55°E36'
39'
42'
45'
48'

Figure 3

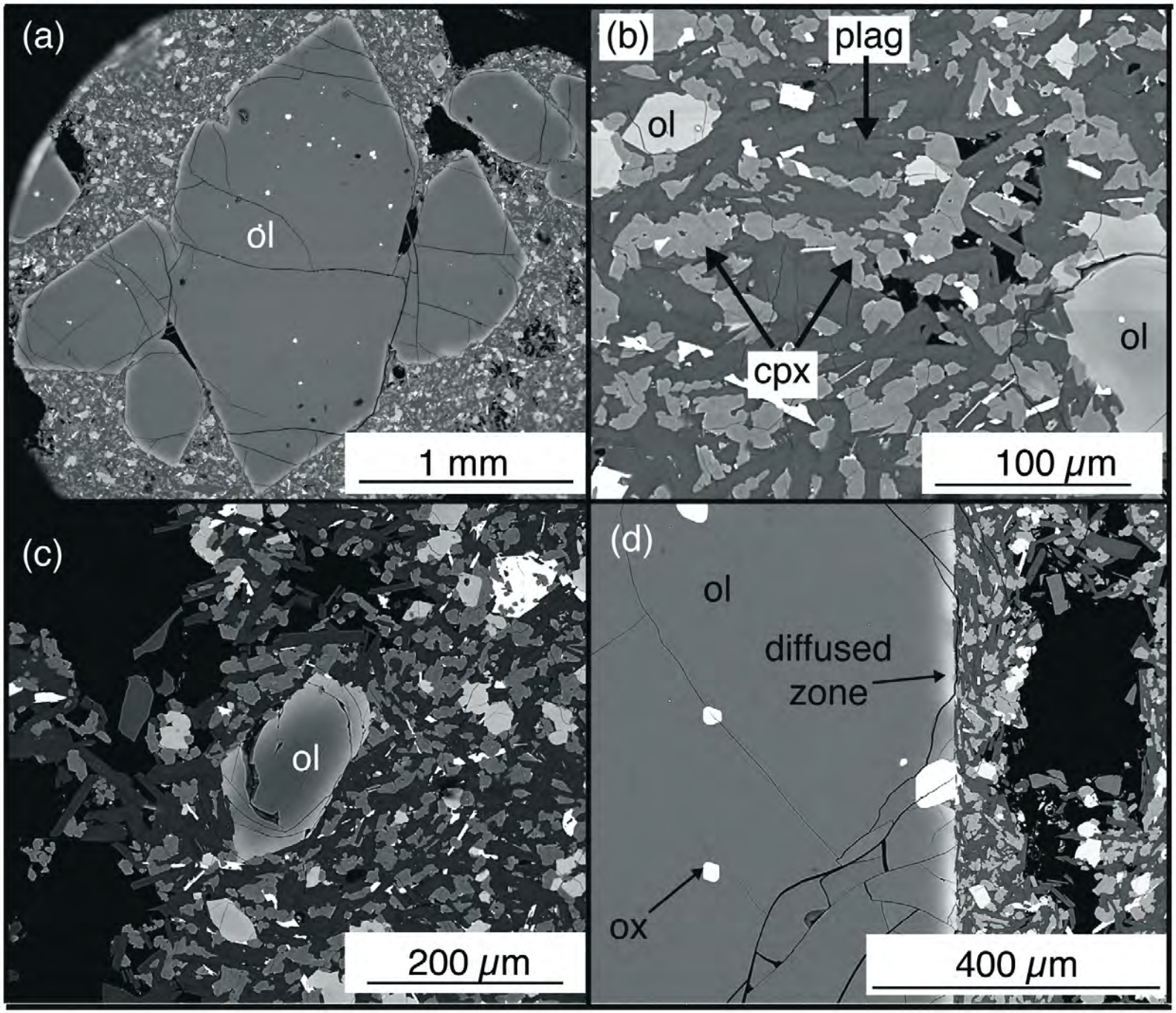
(a)
ol
1 mm
(b)
plag
ol
cpx
ol
100 μm
(c)
ol
200 μm
(d)
ol
diffused
zone
ox
400 μm

Figure 4

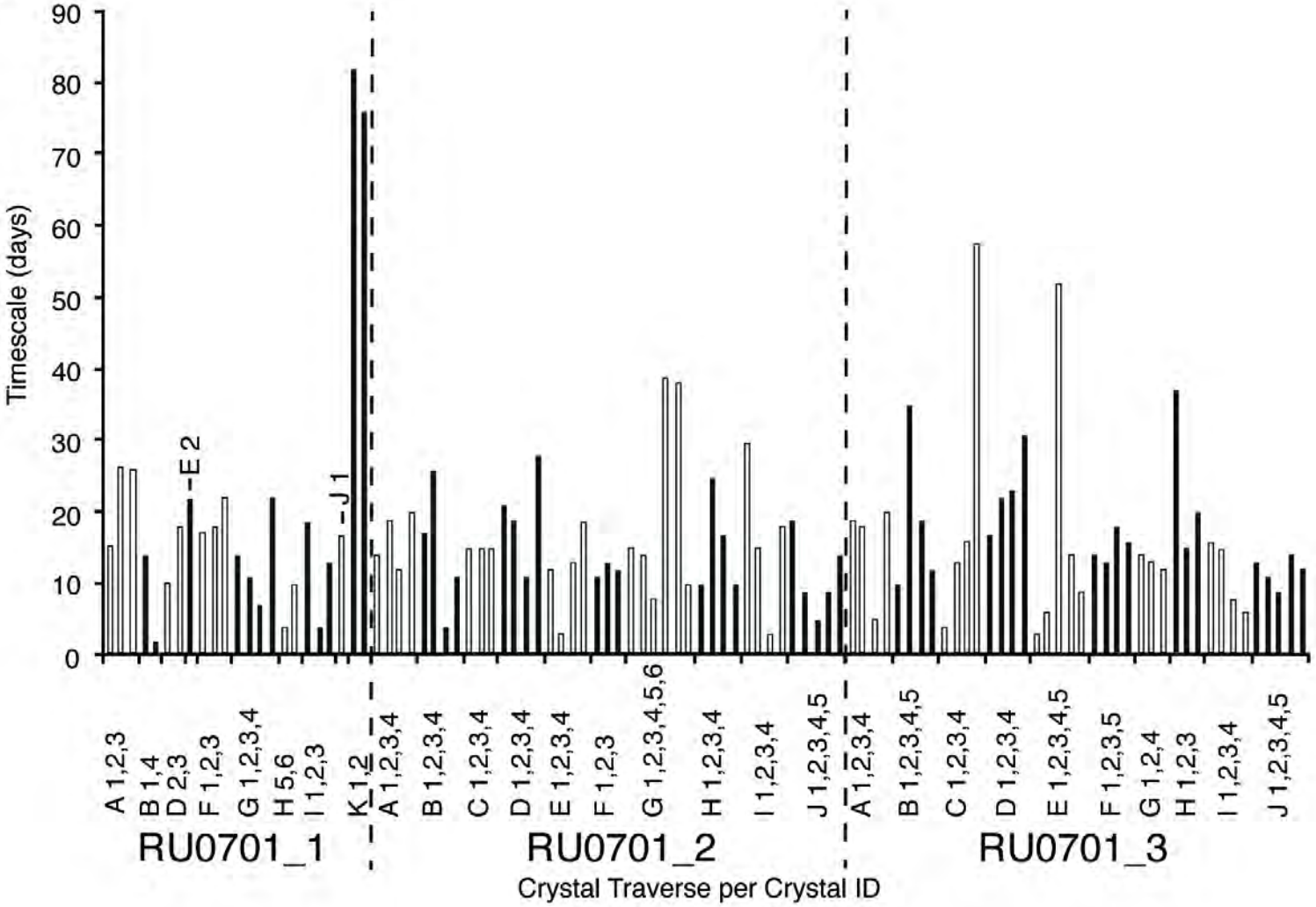
Timescale (days)
90
80
70
60
50
40
30
20
10
0
E 2
J 1
A 1,2,3
B 1,4
D 2,3
F 1,2,3
G 1,2,3,4
H 5,6
I 1,2,3
K 1,2
A 1,2,3,4
B 1,2,3,4
C 1,2,3,4
D 1,2,3,4
E 1,2,3,4
F 1,2,3
G 1,2,3,4,5,6
H 1,2,3,4
I 1,2,3,4
J 1,2,3,4,5
A 1,2,3,4
B 1,2,3,4,5
C 1,2,3,4
D 1,2,3,4
E 1,2,3,4,5
F 1,2,3,5
G 1,2,4
H 1,2,3
I 1,2,3,4
J 1,2,3,4,5
RU0701_1
RU0701_2
RU0701_3
Crystal Traverse per Crystal ID

Figure 5

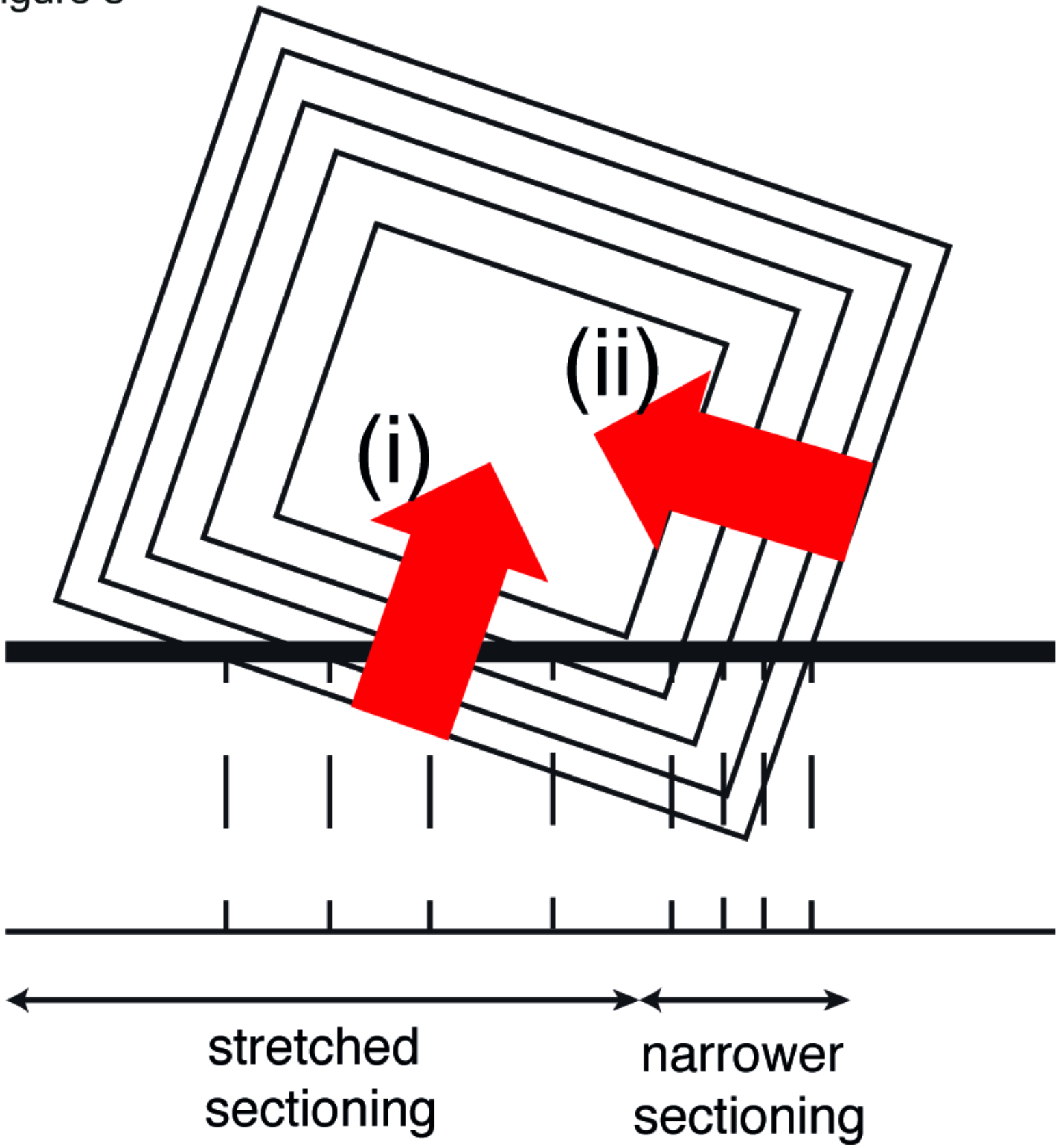

Figure 6

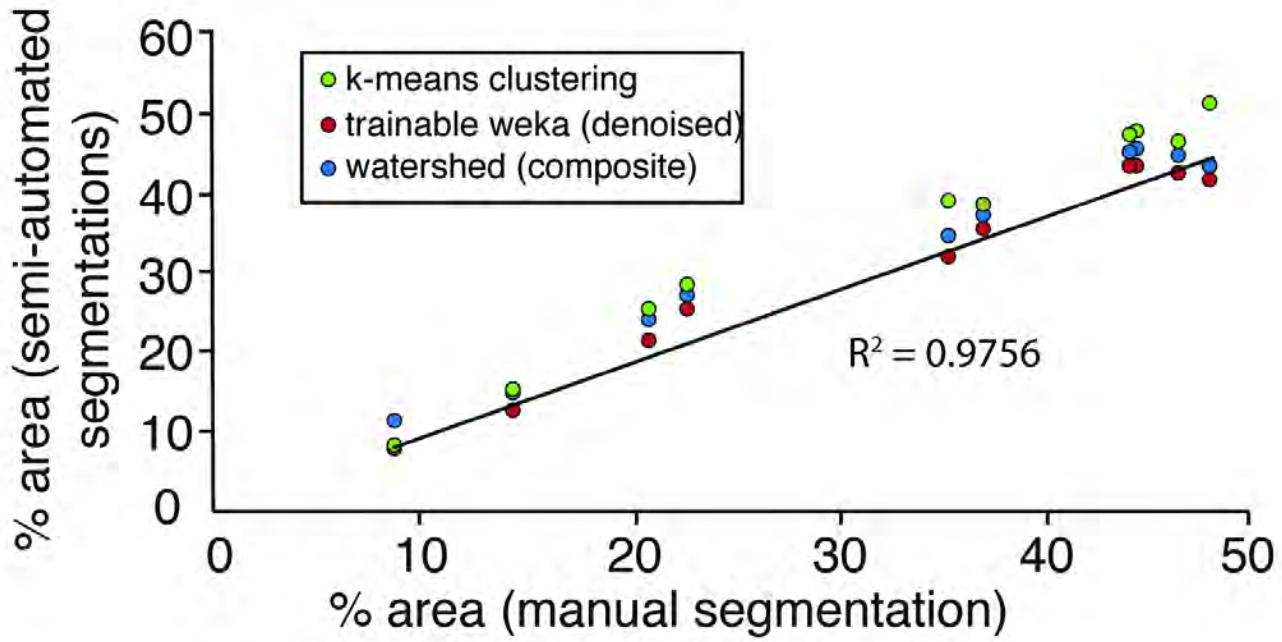
k-means clustering
trainable weka (denoised)
watershed (composite)
$R^2 = 0.9756$
% area (semi-automated segmentations)
% area (manual segmentation)
0
10
20
30
40
50
60

Figure 7

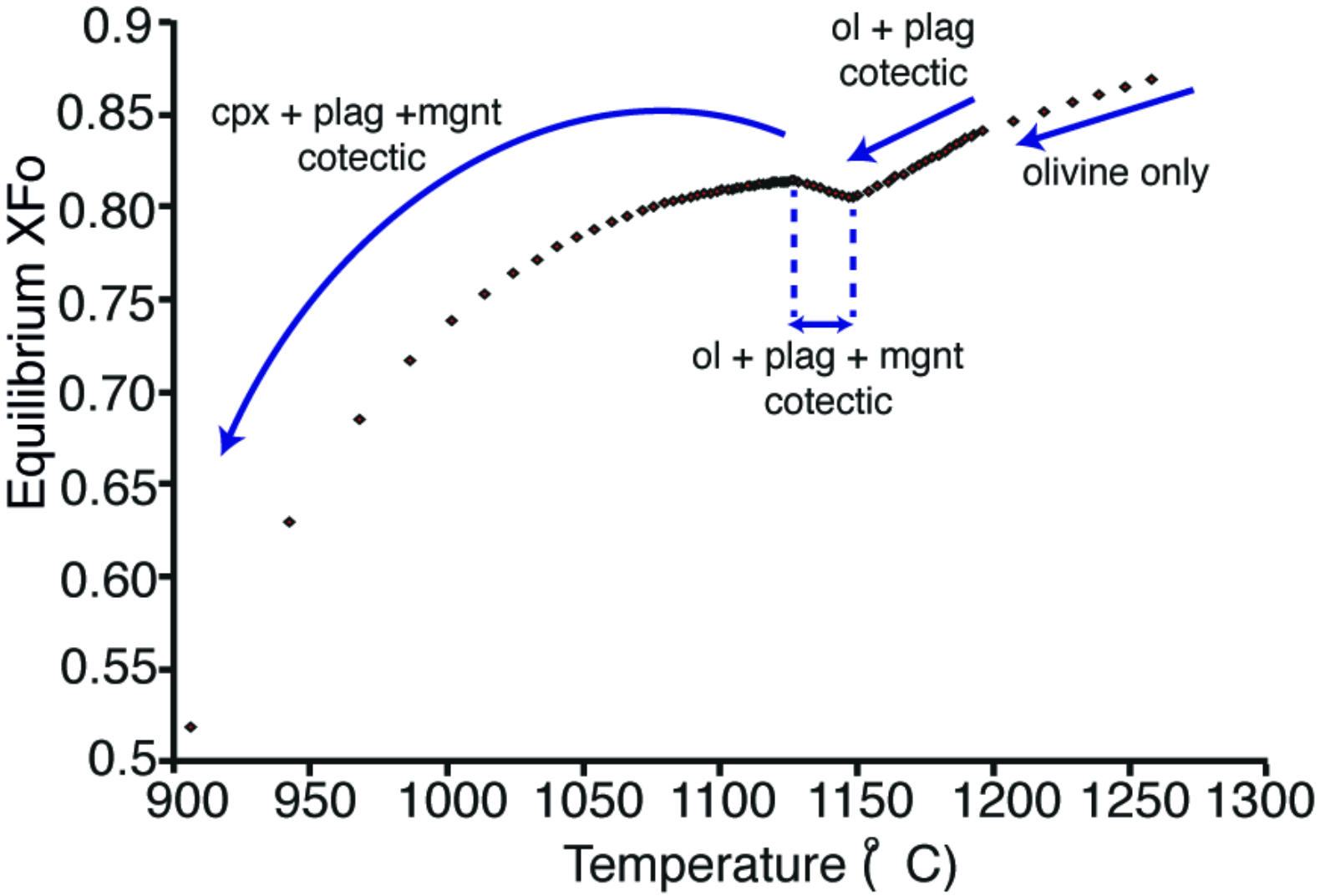
0.9
0.85
0.80
0.75
0.70
0.65
0.60
0.55
0.5
Equilibrium XFo
900
950
1000
1050
1100
1150
1200
1250
1300
Temperature (° C)
cpx + plag +mgnt
cotectic
ol + plag
cotectic
olivine only
ol + plag + mgnt
cotectic

Figure 8

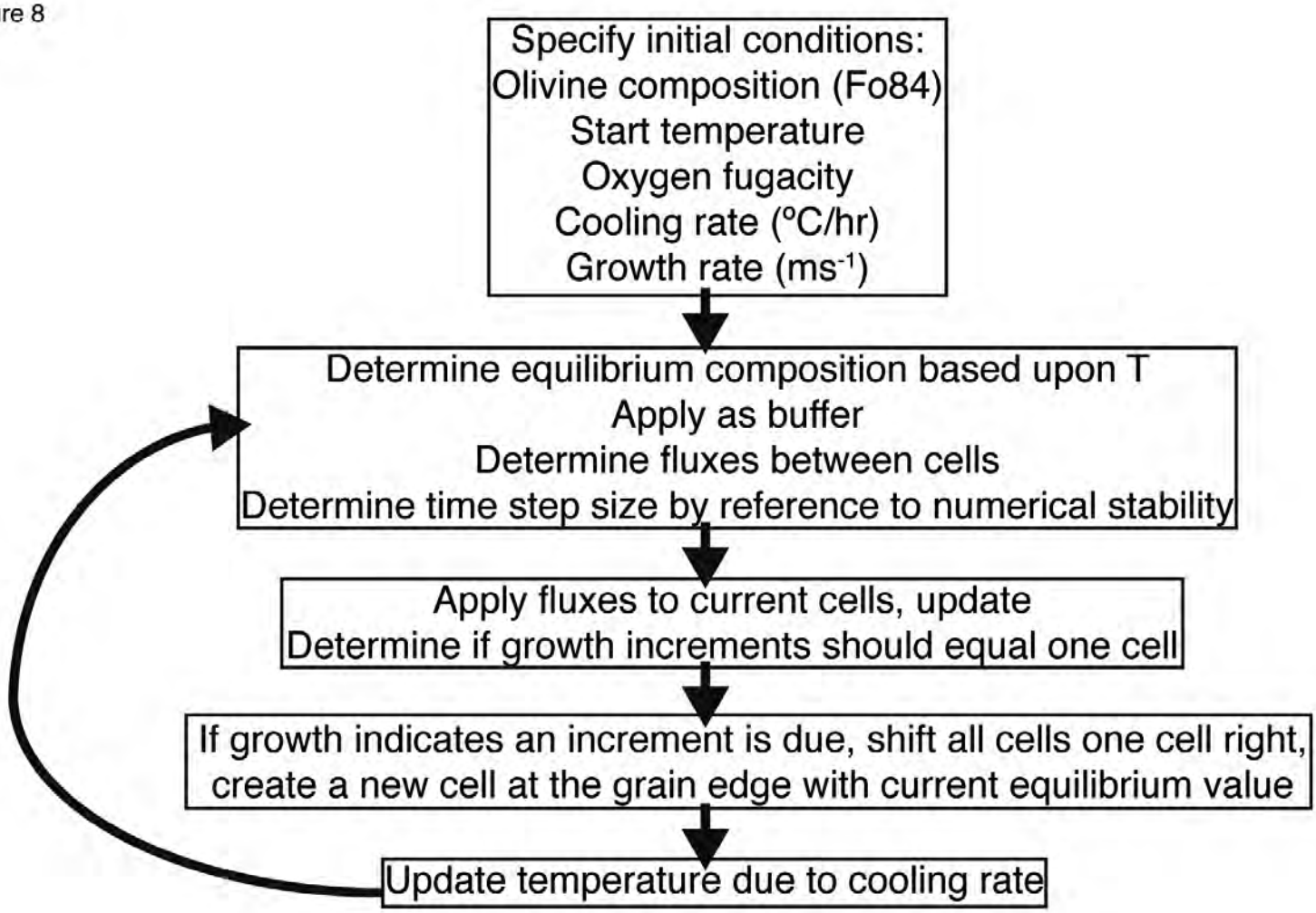
Specify initial conditions:
Olivine composition (Fo84)
Start temperature
Oxygen fugacity
Cooling rate (ºC/hr)
Growth rate (ms-1)
Determine equilibrium composition based upon T
Apply as buffer
Determine fluxes between cells
Determine time step size by reference to numerical stability
Apply fluxes to current cells, update
Determine if growth increments should equal one cell
If growth indicates an increment is due, shift all cells one cell right,
create a new cell at the grain edge with current equilibrium value
Update temperature due to cooling rate

Figure 9

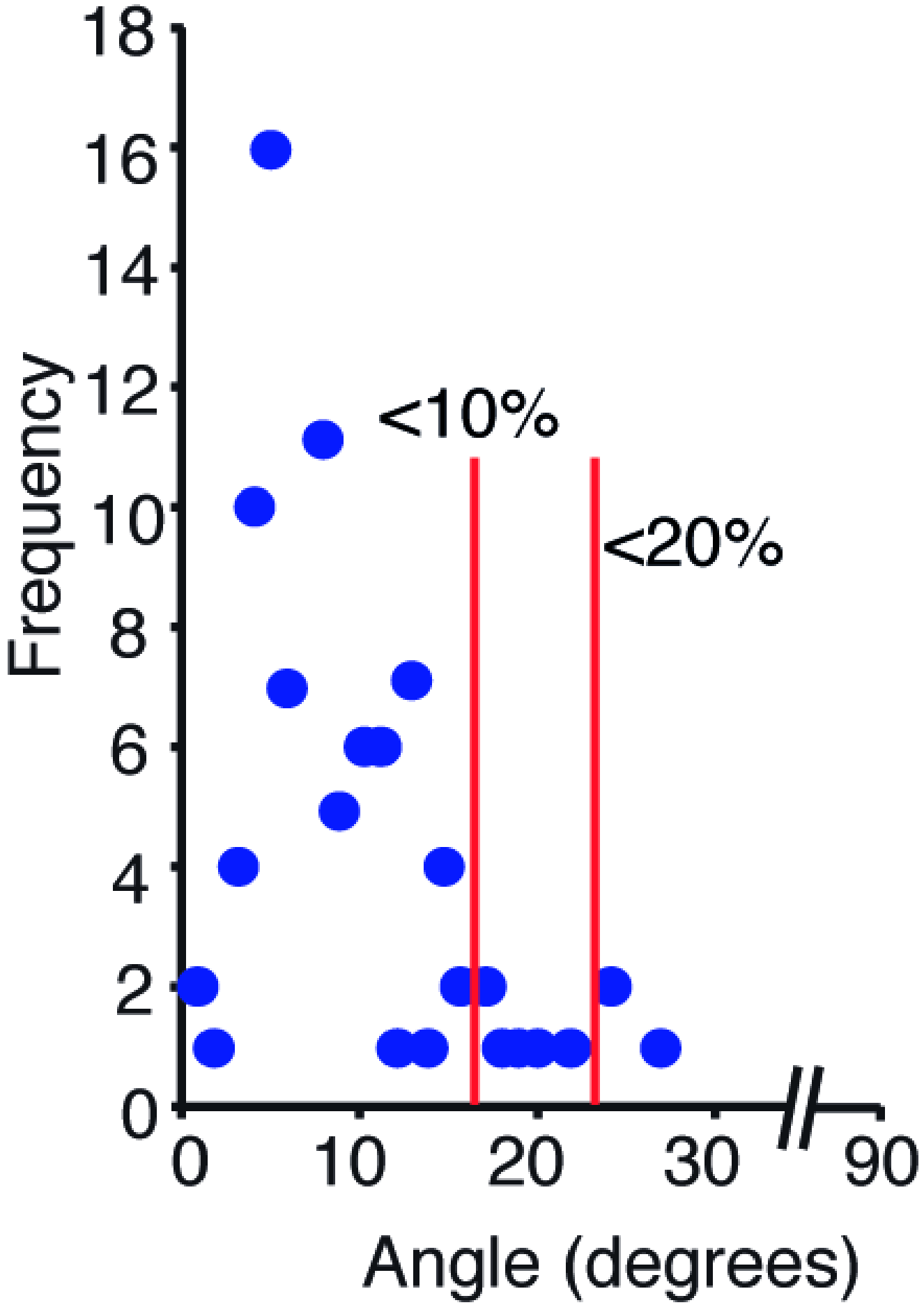

Figure 10

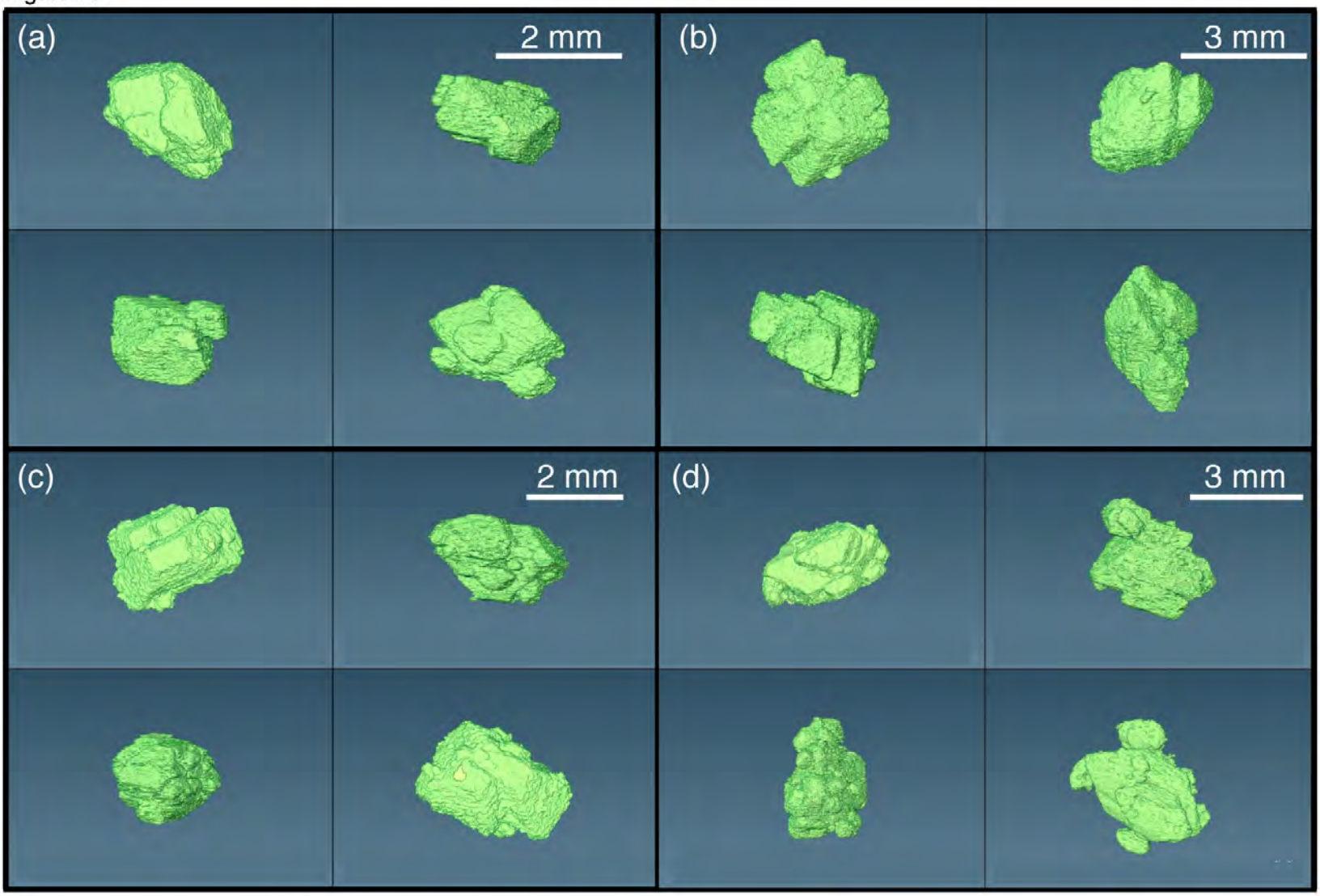
(a)
2 mm
(b)
3 mm
(c)
2 mm
(d)
3 mm

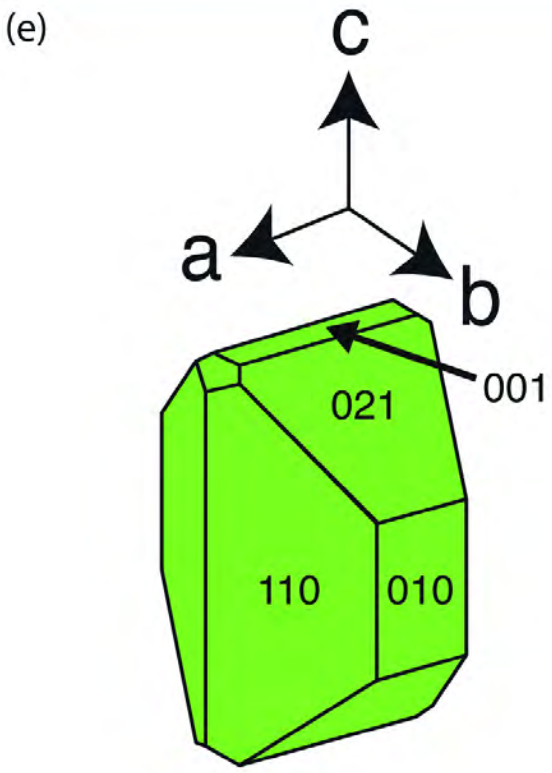
(e)
c
a
b
001
021
110
010

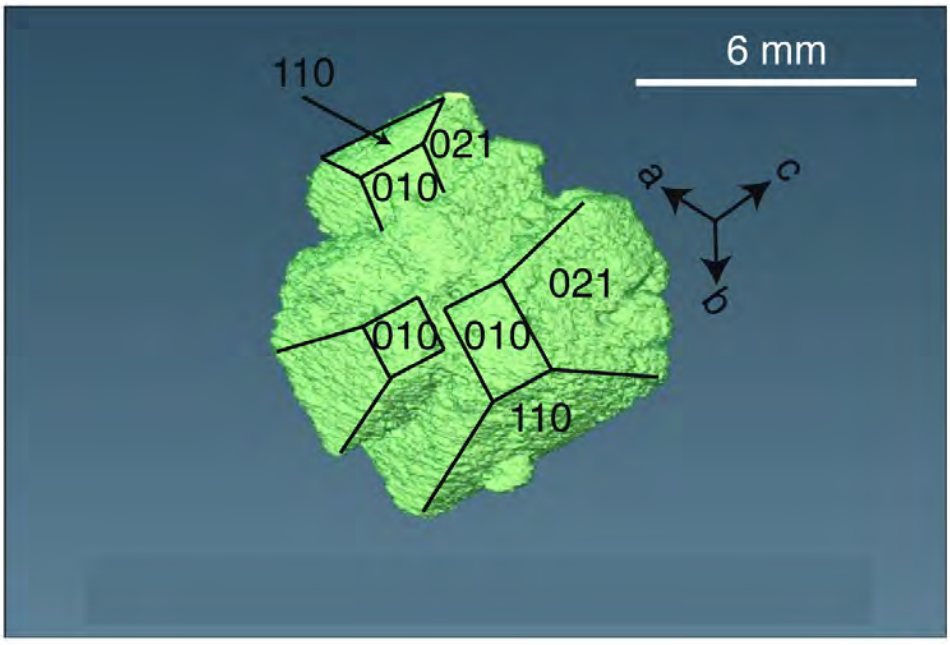
6 mm
110
021
010
021
010
010
110
a
c
b

Figure 11

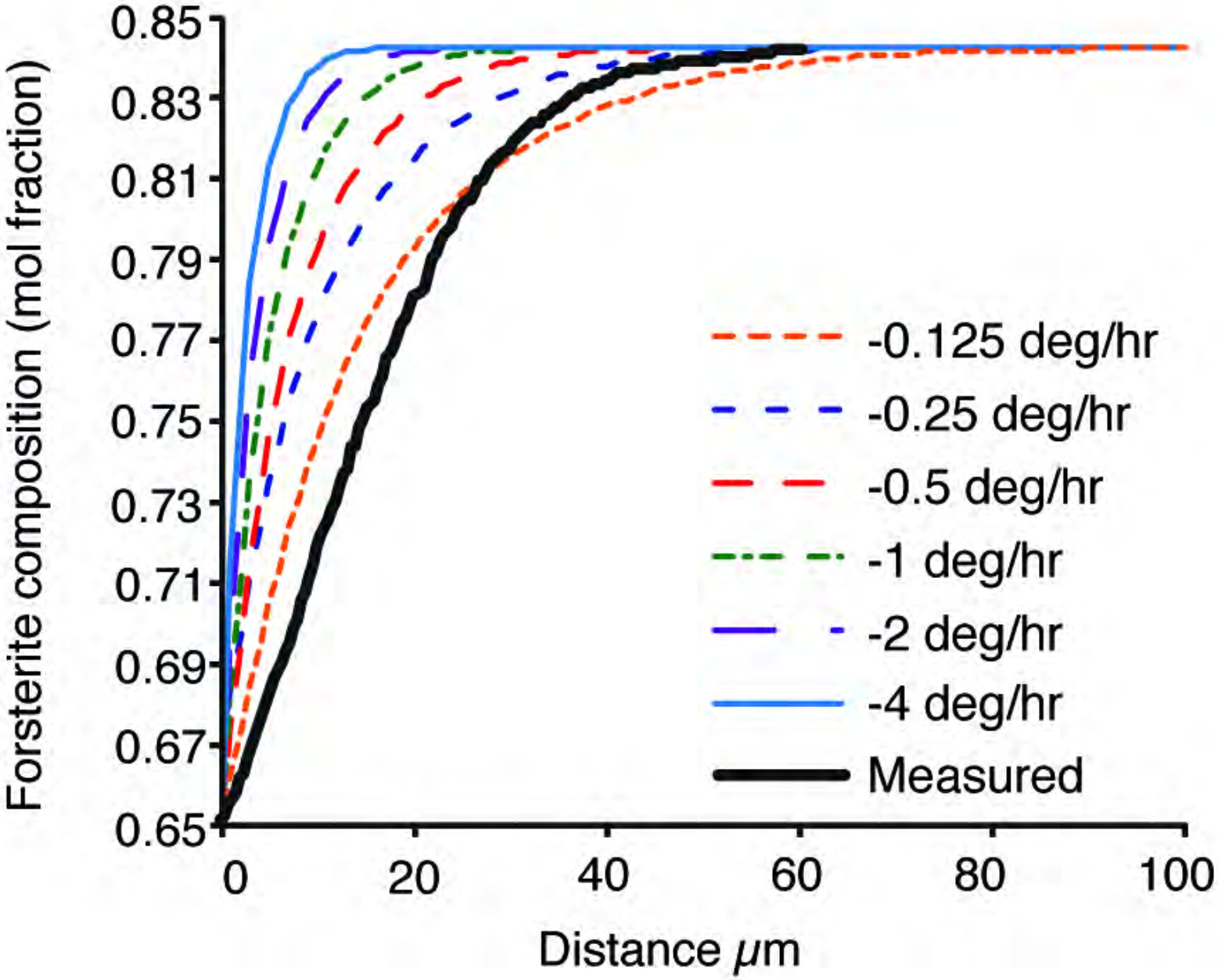
Forsterite composition (mol fraction)
0.85
0.83
0.81
0.79
0.77
0.75
0.73
0.71
0.69
0.67
0.65
0
20
40
60
80
100
Distance μm
-0.125 deg/hr
-0.25 deg/hr
-0.5 deg/hr
-1 deg/hr
-2 deg/hr
-4 deg/hr
Measured

Figure 12

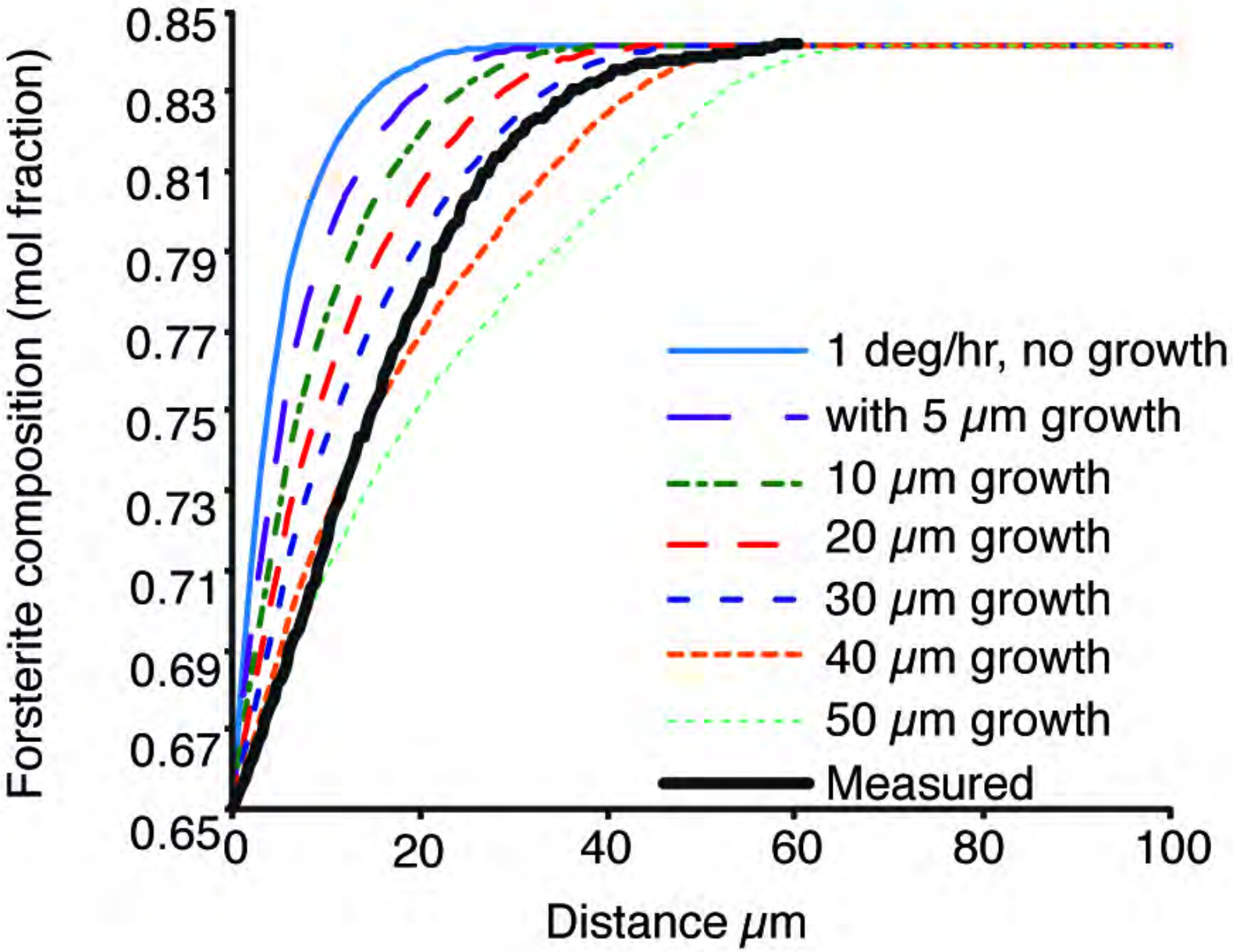
Forsterite composition (mol fraction)
0.85
0.83
0.81
0.79
0.77
0.75
0.73
0.71
0.69
0.67
0.65
0
20
40
60
80
100
Distance μm
1 deg/hr, no growth
with 5 μm growth
10 μm growth
20 μm growth
30 μm growth
40 μm growth
50 μm growth
Measured

Figure 13

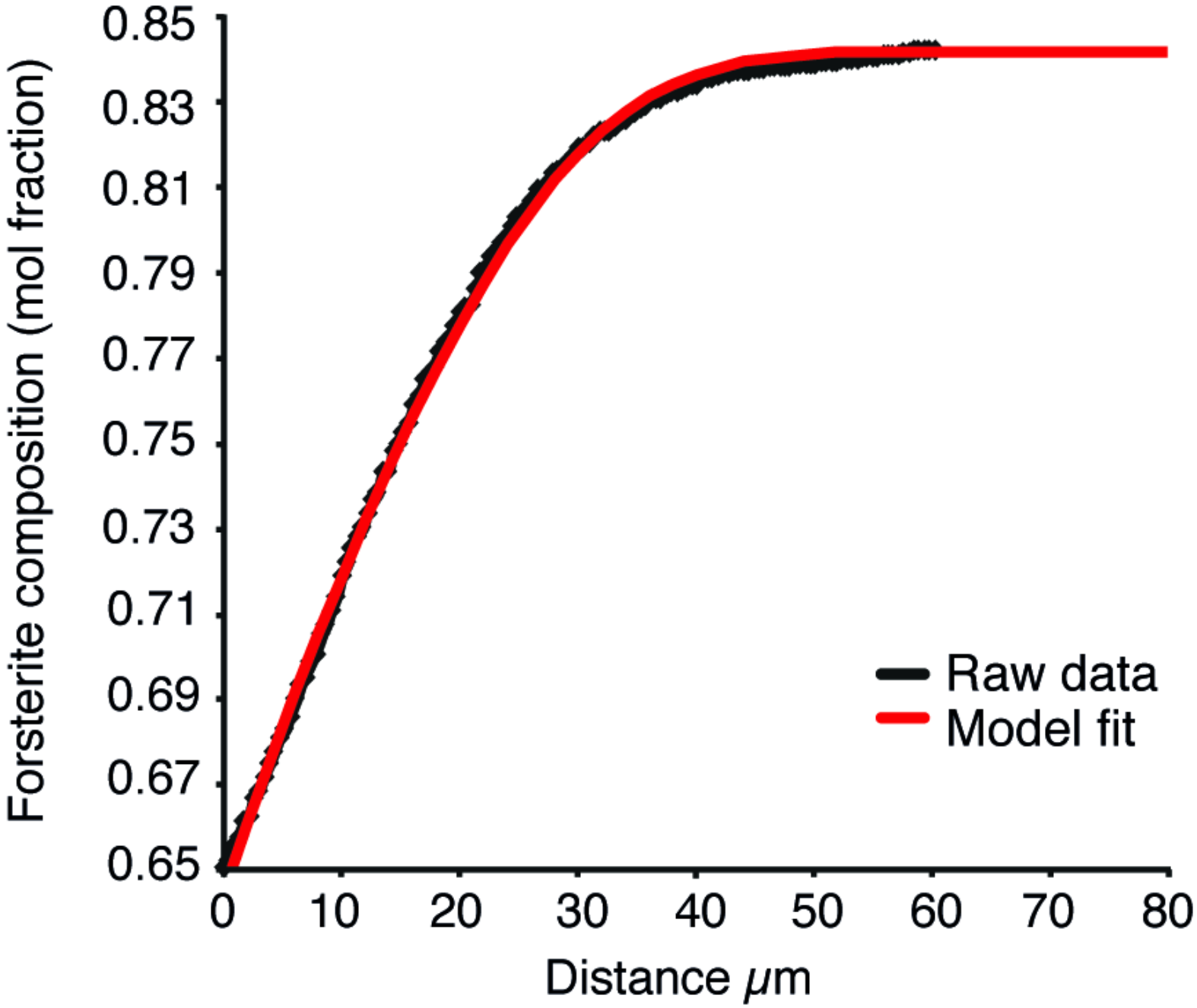
Forsterite composition (mol fraction)
0.85
0.83
0.81
0.79
0.77
0.75
0.73
0.71
0.69
0.67
0.65
0
10
20
30
40
50
60
70
80
Distance μm
Raw data
Model fit

Figure 14

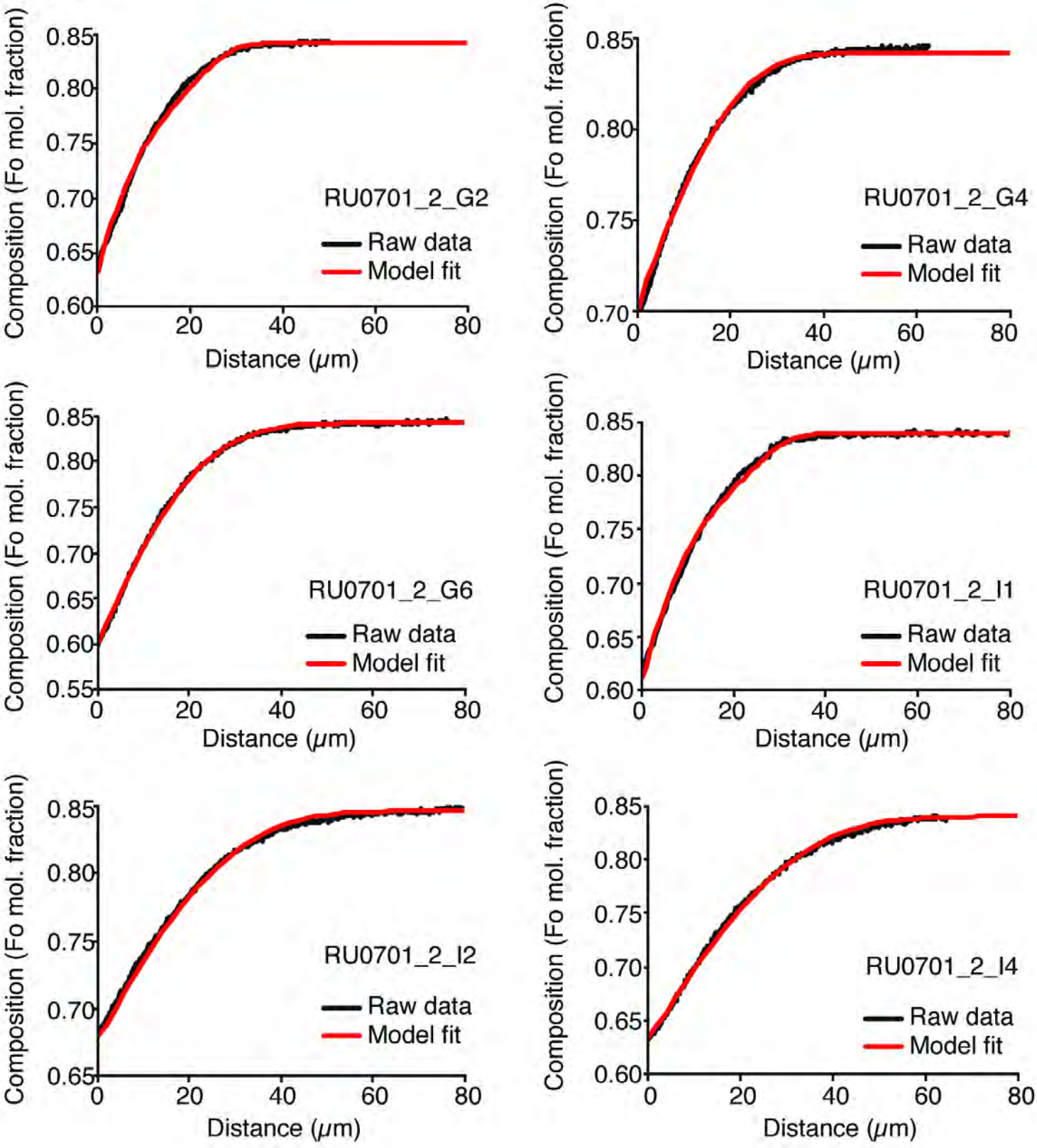
Composition (Fo mol. fraction)
Distance (μm)
RU0701_2_G2
Raw data
Model fit
RU0701_2_G4
RU0701_2_G6
RU0701_2_I1
RU0701_2_I2
RU0701_2_I4

Figure 15

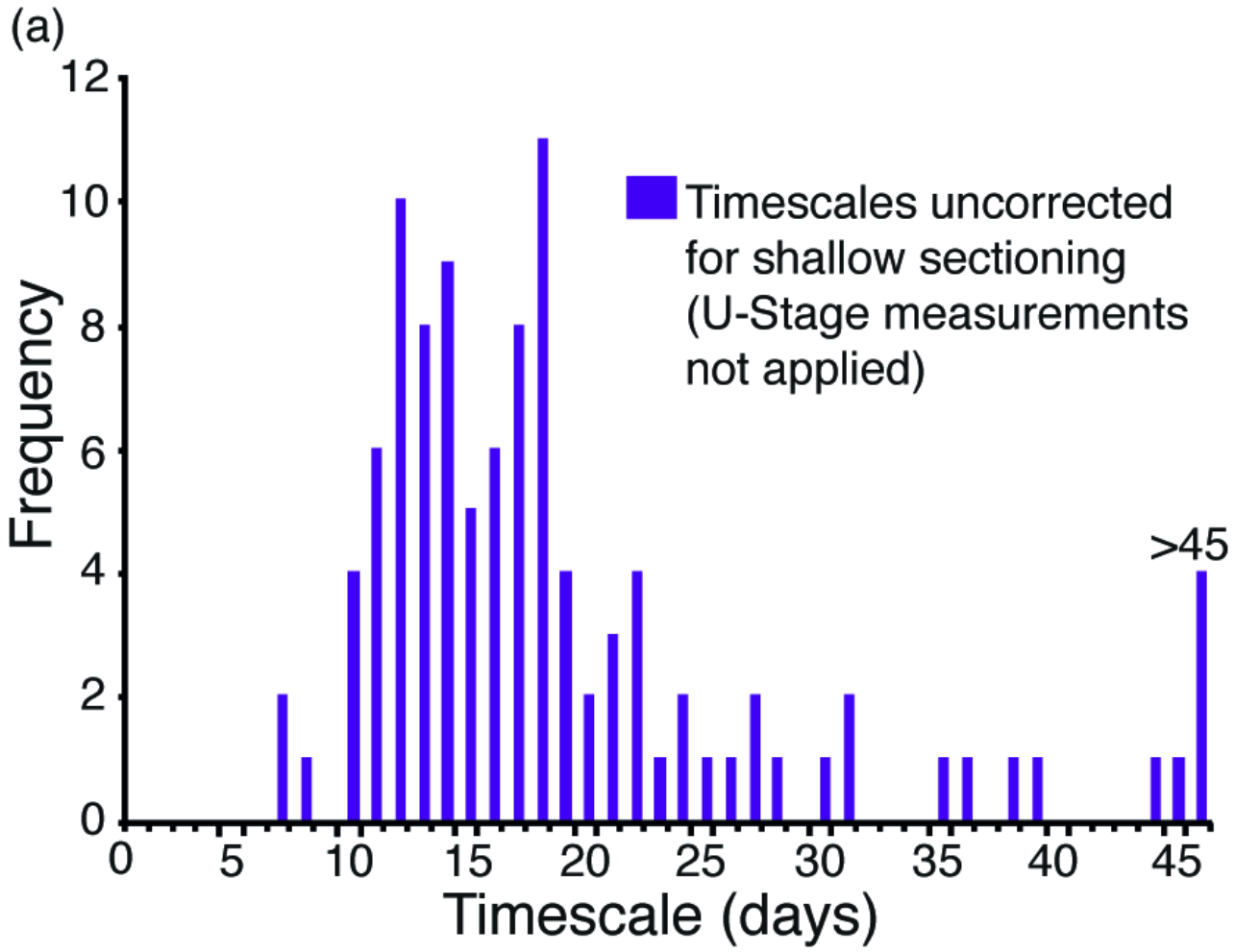
(a)
Frequency
Timescales uncorrected for shallow sectioning (U-Stage measurements not applied)
>45
Timescale (days)
(b)
Frequency
Timescales corrected for shallow sectioning (U-Stage measurements applied
>45
Timescale (days)

Figure 16

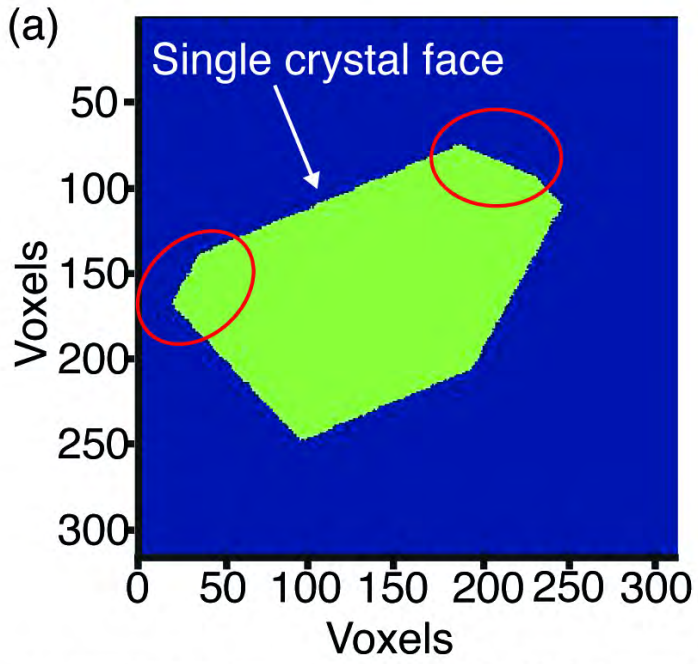
(a)
Single crystal face
50
100
150
200
250
300
Voxels
0
50
100
150
200
250
300
Voxels

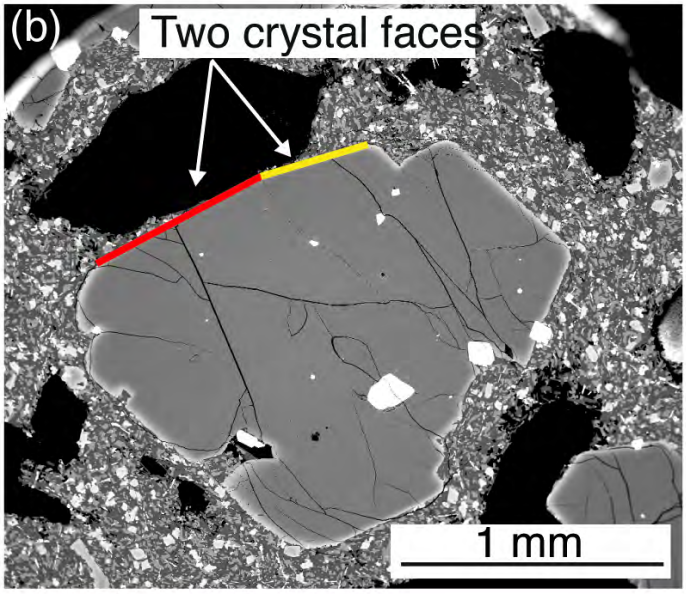
(b)
Two crystal faces
1 mm

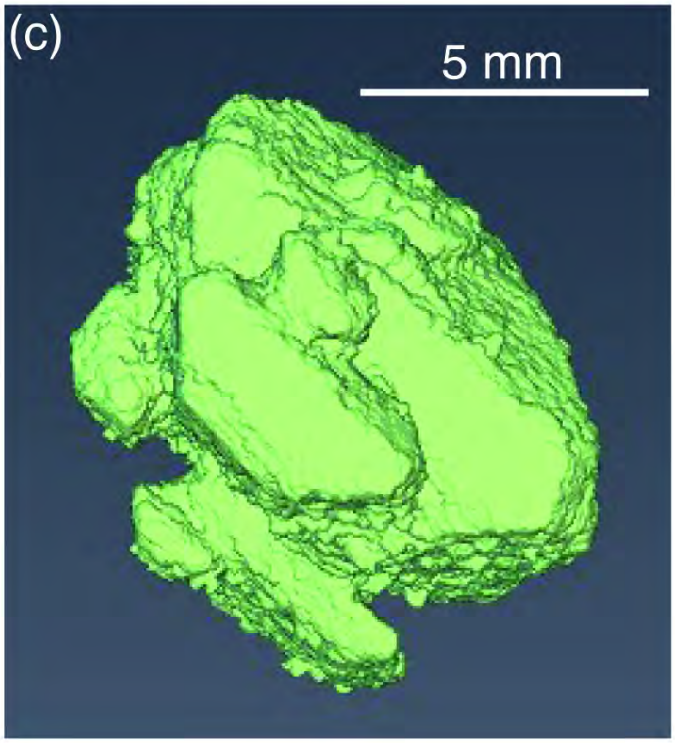
(c)
5 mm